Intraplate volcanism and mantle plume dynamics: results from analogue experiments

$\sim$

Intraplattenvulkanismus und die Dynamik von Mantelplumes: Ergebnisse von Analogexperimenten

DIPLOMARBEIT

vorgelegt der
Fakultät für Mathematik, Informatik und Naturwissenschaften
der Universität Hamburg

Gutachter

Prof. Dr. Matthias Hort
Dr. Jörg Hasenclever

2014
Johann Jacobsohn

Zusammenfassung & Abstract

Zusammenfassung

Energie- und Massentransport durch Manteldiapire (sogenannte „Mantle Plumes“) ist ein wichtiger Prozess innerhalb der thermischen Konvektion des Erdmantels. Numerische Experimente werden erfolgreich verwendet, um Mantelkonvektion im Allgemeinen und Manteldiapire im Besonderen besser zu verstehen und ihre Eigenschaften besser einzugrenzen. Laborexperimente sind ein wichtiges Werkzeug, um numerische Modelle zu testen, zu verifizieren und zu parametrisieren. Nicht viele experimentelle Datensätze wurden bisher veröffentlicht.

In dieser Arbeit wurden sechs Datensätze von thermischen Diapiren in einem sirup-gefüllten Acrylglastank hergestellt und mit Rechnungen des numerischen Konvektionsmodells „M2TRI“ (Hasenclever, 2010) verglichen. Um genaue Modellierung zu ermöglichen, wurden die physikalischen Parameter des Aufbaus und des Sirups bestimmt. Die Experimente wurden mittels „Particle Image Velocimetry (PIV)“ verarbeitet und ihr Flussfeld damit analysiert. Sowohl das Flussfeld als auch die Aufstiegsraten der Experimente und der Modellrechnungen wurden miteinander verglichen. M2TRI wurde erfolgreich eingesetzt, um die gemessenen Diapire innerhalb der Messgenauigkeit zu modellieren. Die Datensätze können vom Institut für Geophysik der Univerversität Hamburg bezogen werden.

Abstract

Plumes are an important feature of Earth’s mantle. Numerical experiments are used to better understand and constrain mantle convection in general and mantle plumes in particular. Analogue laboratory experiments are used to benchmark and parametrise these codes and can help to improve the underlying algorithms. Unfortunately, not many experimental data sets have been published so far.

In this work six data sets of thermal plumes in a sirup-filled acrylic glass tank were produced and tested against the numerical convection code M2TRI (Hasenclever, 2010). To allow exact numerical calculations, the precise physical parameters of the sirup and experimental layout were determined. The experiments were then processed with Particle Image Velocimetry (PIV) to analyse the flow field. The velocity profile and ascent rates of the numerical and experimental plumes were compared. M2TRI was successfully applied to model plumes that are similar within the experimental uncertainties to the plumes generated in the experiments. The data sets are available from the Institute of Geophysics, University of Hamburg.

Contents

1. Introduction

Earth is structured into four basic layers. In the center, a rigid inner core of solid iron is encompassed in a fluid, highly turbulent, molten iron outer core. The core is embedded in Earth's mantle, which is solid, yet—on geological timescales—ductile. On the surface of the mantle lies Earth's crust, which is broken up into tectonic plates (Figure 1.1).

The mantle is divided by the transition zone between 410 and 660 km depth into the lower and upper mantle. It can be further divided into a rigid lithosphere in the upper 200 km, and a ductile (flowable) asthenosphere below.

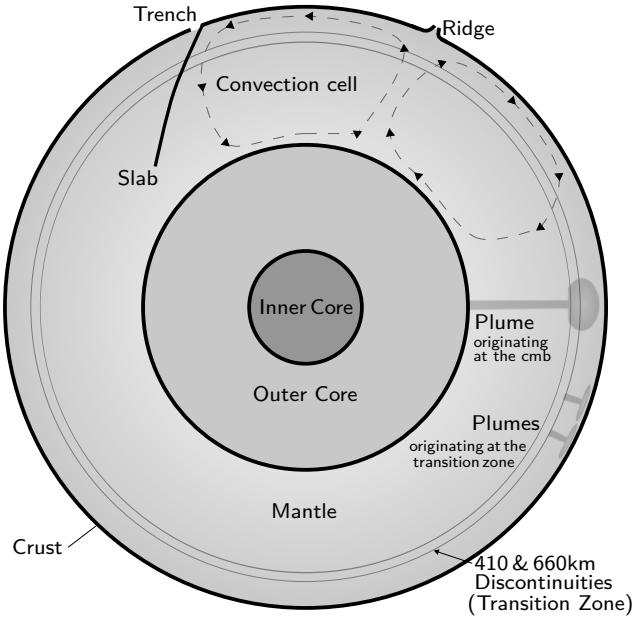

Figure 1.1.: The composition of Earth and major features of Earth's mantle. Earth has a radius of 6371 km and is structured in four layers: in the center, an inner core of 1214 km diameter is embedded in a 3485 km outer core, which is embedded in a 2856 km thick mantle, which is covered by the crust. While the inner core is solid, the outer core is fluid. The mantle is ductile and exhibits thermal convection. The crust is cold, rigid and rather thin: from 6 km for oceanic crust to up to 75 km for continental crust (Schubert et al., 2001). Earth's mantle exhibits large scale convection and smaller scale mantle plumes. These can originate at the core mantle boundary (CMB) or at the transition zone. The sketch is simplified and not to scale.

The mantle's inner processes directly influence the genesis of the crust and processes like volcanism, earth quakes and plate tectonics. A better understanding of the processes in the mantle will yield a better understanding of the processes in the crust. The processes in the mantle are mainly thermally driven.

The thermal budget of Earth's mantle can be attributed almost entirely to radiogenic heating, heating from the core and cooling from the crust. 6–10 TW of thermal power is being transferred from the core to the lower mantle. Radiogenic heating can reasonably be assumed to be isotropic throughout the mantle, and negligible in the core (Schubert et al., 2001). Because the mantle is heated from below (and, to a certain extent, from within) and cooled from above, thermal convection establishes and forms a chaotic state of convection (Ricard, 2007). This convection takes place in large, time-dependent convection cells. It is as yet unclear if the convection in

Earth's mantle is mainly a whole-body or a layered convection (Machetel and Weber, 1991).

The convective drag exerted on the lithospheric plates causes them to break and drift into each other, generally forcing the denser oceanic plates into the mantle. This is known as plate tectonics. The vast majority of volcanism and earth quakes that are seen today are a product of shifting plate boundaries. There are however transient volcanic systems that are not associated with plate boundaries, so-called hotspots.

Hotspots are volcanic systems that cannot be directly linked with plate tectonics. They typically exhibit topographic swell (a regional topograhic high) and so-called hot spot tracks (chains of now inactive volcanic mounts), both pointing to a plate-independent mechanism. It is noteworthy that magma expelled by hotspot volcanism is compositionally different from magma found in volcanism associated with subduction zones (i.e. volcanic arcs), indicating that they have a different source mechanism (Schubert et al., 2001). Prominent examples include Hawaii, Yellowstone and the Canaries.

Forty years ago, Morgan (1971) suggested that these hotspots are caused by a rapid upwelling of a diapir-like structures of hot material, named mantle plumes. This theory is consistent with the formation of hotspot trails, their transient nature and the formation of hotspot swells. Both numerical as well as lab studies predict the formation of plumes (Nataf, 2000).

It is as of yet unclear where mantle plumes originate, but there is strong evidence that the source lies deeper than the mantle convection cells (Schubert et al., 2001) and there is strong correlation between hot spots and ultra low velocity zones at the core-mantle boundary (CMB), which implies that—at least some—mantle plumes originate at the CMB. While the theory of mantle plumes is still somewhat controversial, it is currently the most viable one. Because it is difficult to detect mantle plumes directly, most arguments are of an indirect nature, but in recent years tomographic seismology has been successfully applied to detect plume-like structures below Iceland (Wolfe et al., 1997; Allen, 2002), Yellowstone (Smith et al., 2009) and other hotspots.

To better understand and constrain this problem, numerical codes have been developed to model Earth's mantle in general and plumes in particular. Hasenclever (2010) and Hasenclever et al. (2011) published two new models (M2TRI for 2d and M3TET for 3d) as part of the SPP 1144 project which are finite element (FEM) codes for mantle convection. It is desirable for these numerical studies to be benchmarked against either analytical solutions of simple fluid-dynamical problems or actual measurements.

Analogue laboratory experiments have a proud history in geophysical research to test hypotheses, provide benchmark data, spark new theories and ideas and constrain physical phenomena. They are especially useful to test numerical studies of volcanic systems, since their internal processes are difficult to measure in situ.

In this work, plumes are generated in heated sirup in a narrow tank. The upwelling is generated solely by a heating element at the bottom center of the tank, and not by introducing a quantity of hot sirup at the base of the tank, as has been done in other works, e.g. Kühnel (2011). This has the benefit of being easier to model in a numerical study and provides a simpler experimental setup which is more reliable and repeatable. The precise setup of the experiment is discussed in 2.1 Experimental tank.

Similar experiments to the ones described in this work have been done by Davaille and Vatteville (2005); Limare et al. (2008); Davaille et al. (2011); Vatteville et al. (2009); Lohmann (2005) and

others. This work builds on the work of Kühnel (2011). It aims at improving the methodological approach and thereby reduce the experimental uncertainties.
Thus, the ambition of this work is twofold:

- To **generate a data set** with which future numerical studies can be benchmarked,
- To **test the M2TRI and M3TET models** with these data sets.

It should be noted that mantle plumes do not look like the experiments presented in this work, they most likely have a very different source mechanism, flow behaviour, and evolution than sirup plumes. Many other effects which are relevant are not modelled as well: mantle wind, phase transition, local topography, and difference in composition of plume to the surrounding mantle material are not present in these experiments. Hence it is not the intention of this work to adequately model all the physical phenomena and parameters in a mantle plume; but rather to produce tightly controlled laboratory experiments, which can be used to validate the fluid-dynamical part of convection codes.

2. Experimental Setup

In this chapter the experimental setup is discussed, the equipment introduced and some basic measurements are described.

2.1. Experimental tank

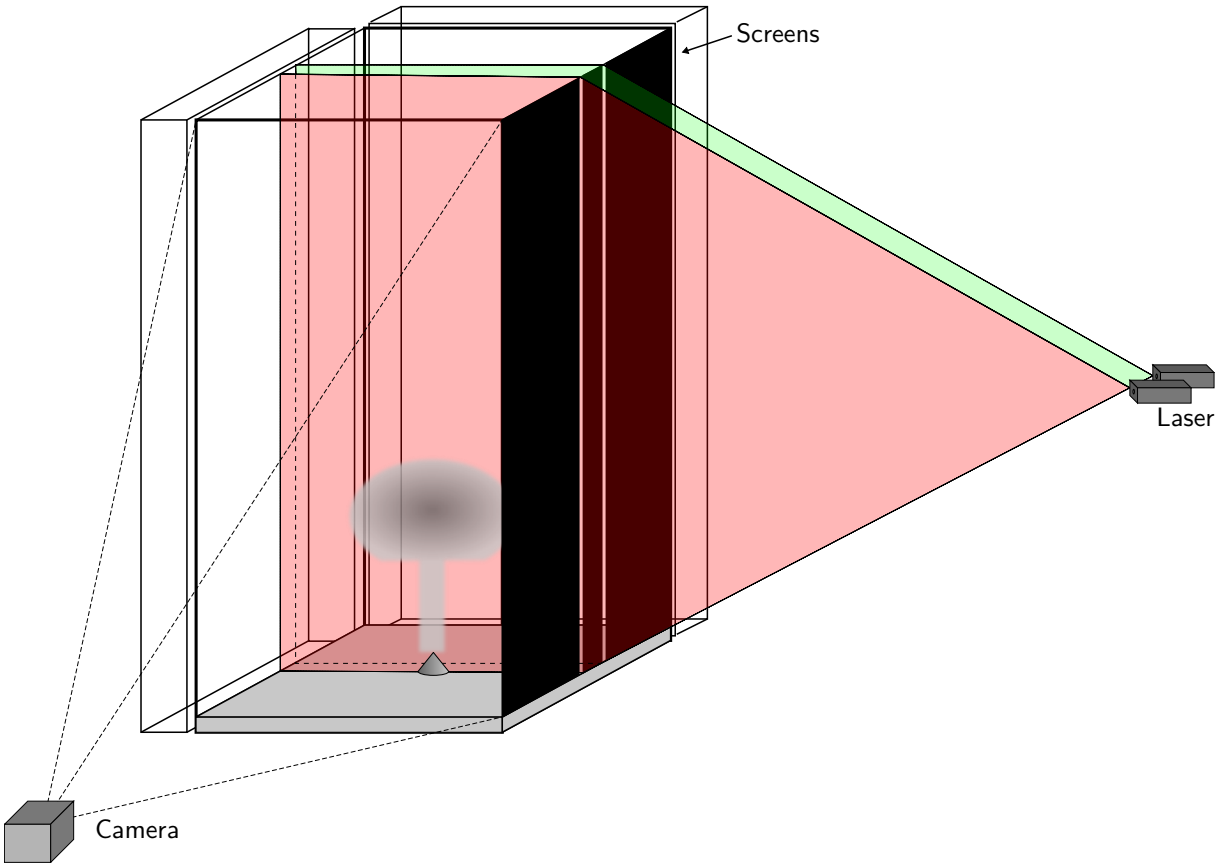

Figure 2.1.: Experimental layout overview. Drawing is approximately to scale, but the water jacket is omited for clearity. The laser light beams are widened to a plane using a sheet optic.

The experiments are set up in an acrylic glass tank with an integrated water jacket that encompasses all four sides of the tank. The water jacket is connected to a regulated water bath that sets a stable background temperature. The tanks inner dimensions are 200 (width) by 200

(depth) by 400 mm (height) with an error of approximately 1mm for width and depth and 10 mm for height (due to variable filling level). The top is insulated with 100 mm styrofoam (EPS) and a 10 mm acrylic glass plate; the bottom is insulated with 20 mm styrofoam (XPS) and a 10 mm acrylic glass plate.

The tank is fitted with 13 temperature probes to measure the background temperature field in-situ (see 2.2 Thermocouples).

A heating element is used to generate thermal plumes and is connected to an oil-filled heated bath. The heating element is a right circular cone in the exact centre of the bottom insulation (± 1 mm), with a radius of 7.5 mm and 10 mm height made from copper and painted matt black with a rough surface. A thermocouple is embedded between the metal of the element and the surrounding insulation. Thermographic images verify that the thermocouple's measured temperature is in agreement with the heating elements temperature and that the element is heated uniformly.

Another thermocouple is placed approximately 10 mm above the tip of the heating element. On the bottom isolation a metal plate of 1mm thickness is placed to secure the insulation and guarantee a flat surface. The plate is not connected to the heating element, thermographic images confirm that the metal plate is not influenced by the heating element. The tank is

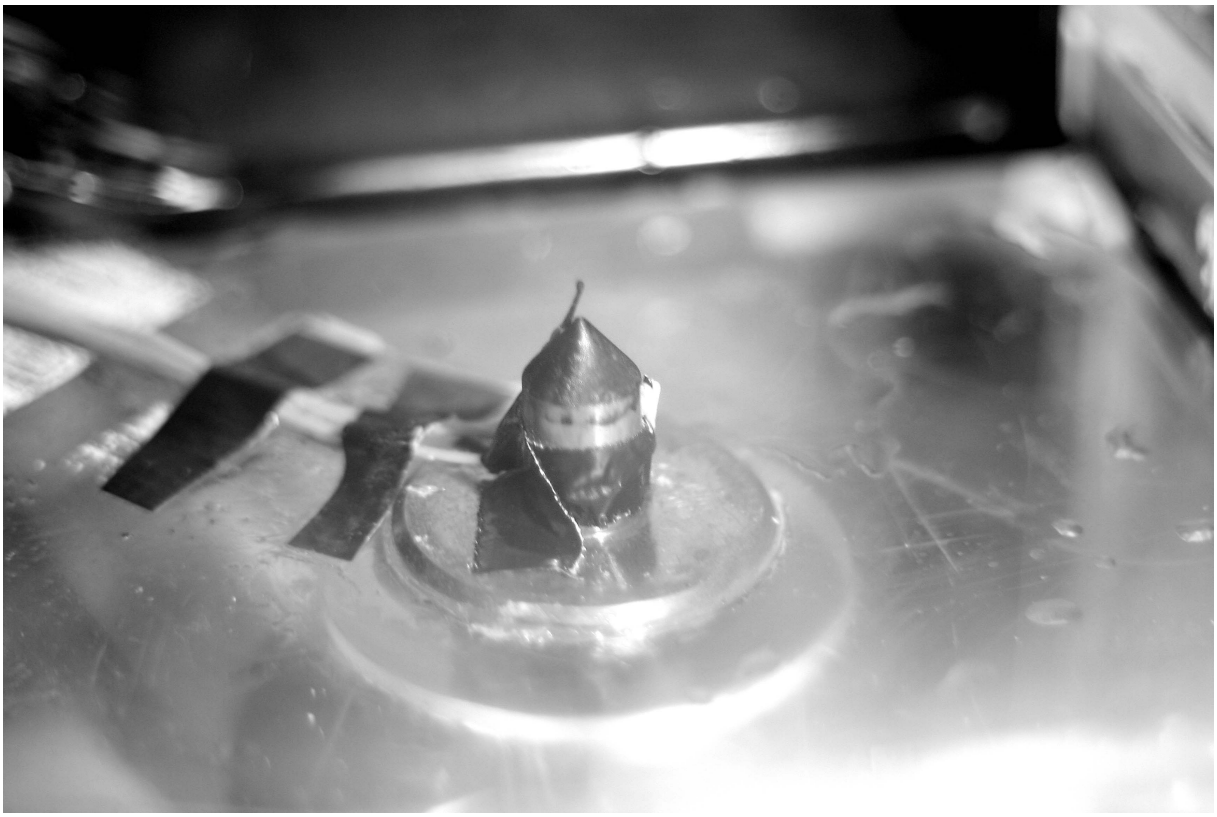

Figure 2.2.: Close-up of the heating element, with isolation removed. Notice the two thermocouples measuring the temperature of and slightly above the heating element. See Figure 3.3 on page 49 for a view of the element during the measurements.

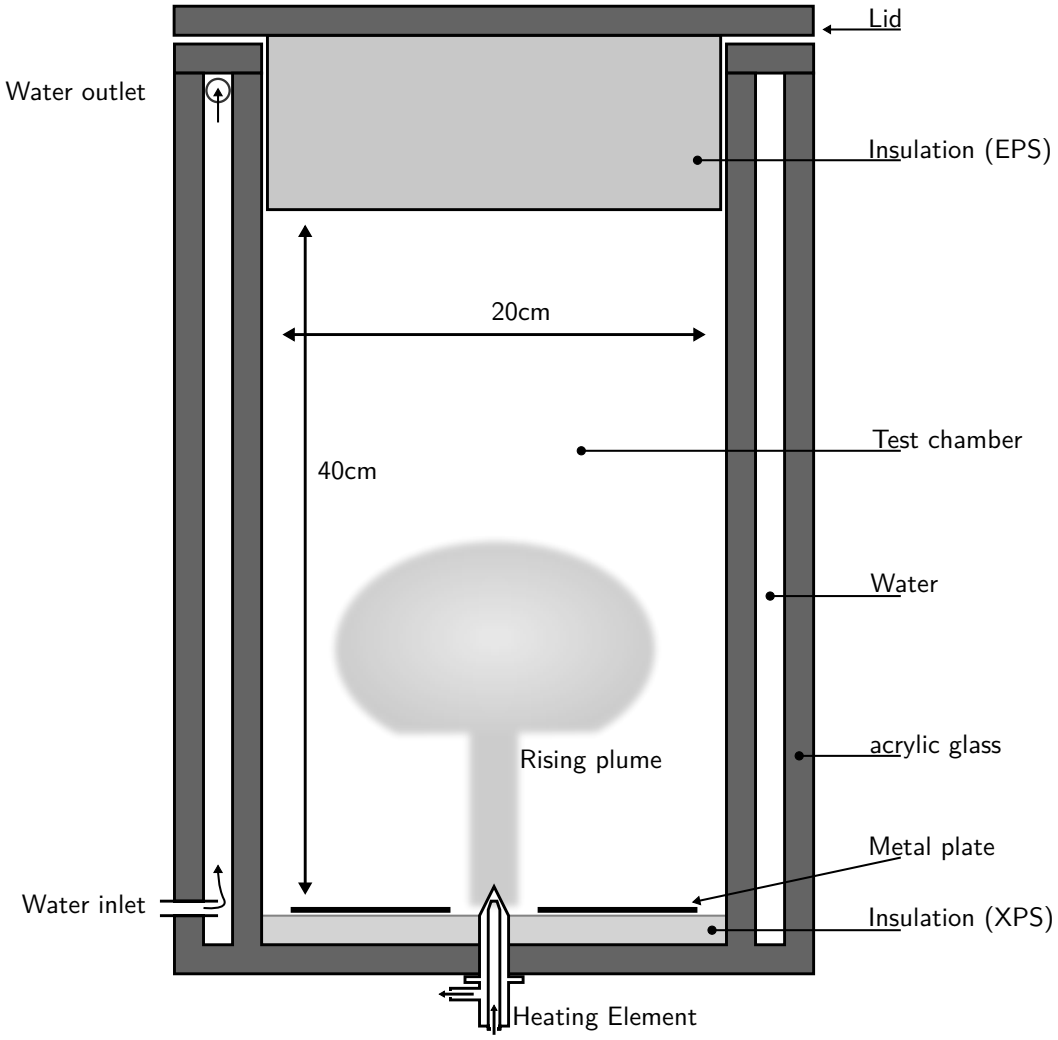

Figure 2.3.: Slightly simplified cross-sectional view of the tank. Drawing not to scale. Contrary to the drawing, the lid fits tightly. The uncommon flow direction in the water jacket helps to remove air. Observation suggests that the water is well mixed, due to the high flow rate. When the heating element is active, a plume of hot sirup forms.

insulated from the outside with aluminium foil and several centimetres of styrofoam on all sides except the sides facing the lasers and camera. All sides, except the one facing the camera, are masked by using black film or paint to reduce unwanted reflection, leaving only small slits for the lasers. The tank is closed with a lid which includes 100 mm of EPS insulation and fits air tight. It includes 5 thermocouples that protrude approximately 5mm into the sirup from above.

Two lasers (see 2.6 Laser) are set up to illuminate two thin vertical planes in the tank and are positioned approximately 60 cm from the tank. Perpendicular to these planes and approximately 1 m from the tank two cameras (see 2.7 Camera) are set up to take the measurements (Figure 2.1 on page 11).

2.2. Thermocouples

The experimental tank is fitted with temperature probes to measure the temperature field in-situ. These probes are so-called thermocouples, which are easy to handle, do not necessarily need to be calibrated and are small enough to be of negligible impact on the flow field. Since the thermocouples are used in a non-aggressive environment (low temperatures and non-aggressive surroundings) ageing effects are not to be expected.

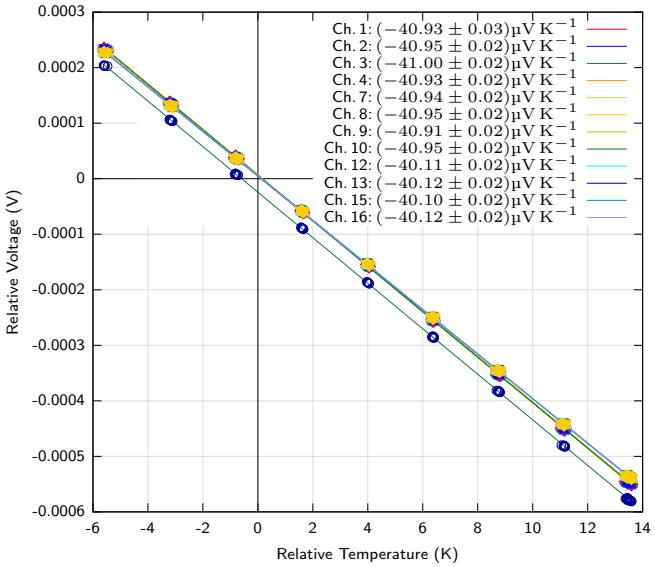

Figure 2.4.: Thermocouple calibration. The differential temperature between hot and cold junction is measured by submerging the hot junction into a thermally controlled bath and is plotted against the induced voltage. For type K thermocouples, a standard correlation factor of $F = 41\,\mu\mathrm{V\,K^{-1}}$ and a functional relationship of $V = F \cdot \Delta T$ can be used, or the exact correlation factor and offset can be measured, yielding considerably improved precision. The channel number corresponds to the numbers used in Table 2.1 and Figure 2.5. Channel 14 was faulty in these measurement and was calibrated separately.

Thermocouples operate by measuring the voltage induced by the thermoelectric or Seebeck effect between two metal wires of different composition, which are connected at two points: the "hot" junction is where the temperature is to be measured, while the "cold" junction is at a known temperature. At the cold junction the latent voltage is precisely read. The Seebeck effect is temperature-dependent and results in a potential that is linear to the temperature difference of hot and cold junction. The same voltmeter is used to measure multiple thermocouples by switching through different channels in quick succession. Because this involves physically changing channels, this limits the temporal resolution.

The Seebeck effect can only be employed to measure the differential temperature between the junctions; to calculate the absolute temperature of the "hot" junction, the absolute temperature of the "cold" junction has to be known. The cold junction can be either cooled to a fixed temperature (e.g. by submerging in ice-water), or constantly measured (e.g. with a PT100 thermometer). The later approach is known as "cold junction compensation" and is used in this work. Additionally, both methods can be combined by measuring e.g. ice-water on an unused channel, which can later be used to correct faulty readings.

The temperatures for each thermoprobe are obtained using

$$T_{hot} = T_{cold} + F \cdot V \tag{2.1}$$

with T_{hot} being the temperature of the hot junction (i.e. the subject of the study), T_{cold} the

(known) temperature of the cold junction and F a proportional factor. For this work, "Type K" thermocouples are employed. Their proportionality factor F is about $41\,\mu V\,K^{-1}$. To reduce the margin of error (which for type K can be put in the range of $\pm 1.5K$), the actual functional relationship between temperature difference and voltage can be assessed, and measured more precisely (Figure 2.4 on page 14).

The experimental tank is fitted with thirteen thermocouples with an instrument error of ± 0.14K: five at the top, seated in the tanks lid, one slightly above the heating element, one at the base of the heating element and six at two of the edges of the tank (Figure 2.5). A detailed account of all thermoprobes is given in Table 2.1.

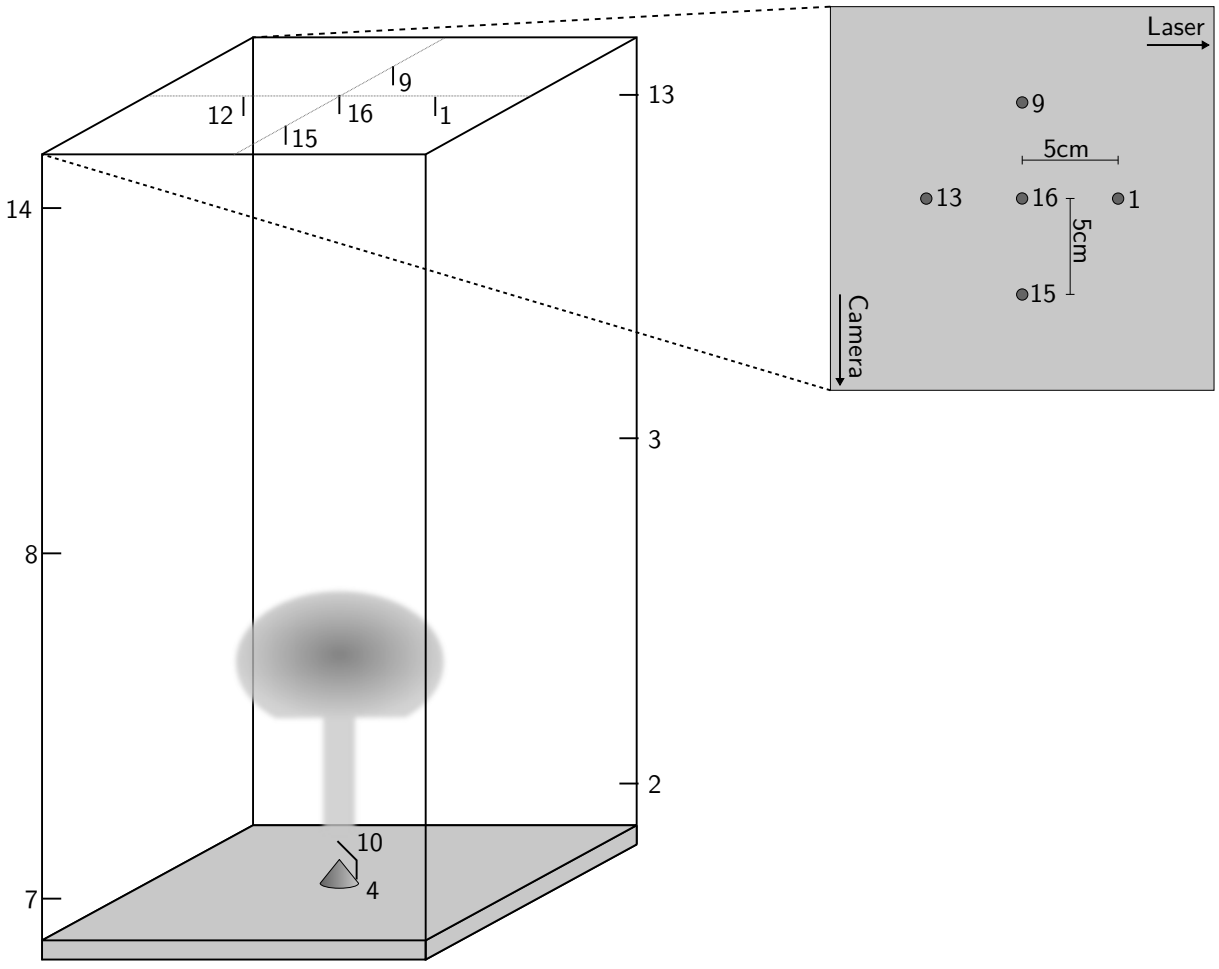

Figure 2.5.: Thermocouple locations. Drawing is approximately to scale. Thirteen thermocouples are placed in the tank. Six are placed in two edges, two at and above the heating element and five in the lid.

Channel #	Position	Coordinates [x;y;z] (m)
	Top	
16	Top center	[.40; 0; 0]
9	Top back	[.40; 0; .05]
15	Top front	[.40; 0; -.05]
12	Top left	[.40; -.05; 0]
1	Top right	[.40; .05; 0]
	Front left	
7	Front left bottom	[.02; -.1; -.1]
8	Front left centre	[.20; -.1; -.1]
14	Front left top	[.38; -.1; -.1]
	Back right	
2	Back right bottom	[.02; .1; .1]
3	Back right centre	[.20; .1; .1]
13	Back right top	[.38; .1; .1]
	Bottom	
4	embedded at the base of the heater	[0; 0; 0]
10	slightly above the heater	[.03; 0; 0]

Table 2.1.: Thermocouple locations. The coordinates are expressed in a right hand coordinate system originating in the centre of the heating element, with the x-axis towards the laser, the y-axis towards the camera, and the z-axis upwards. Position error $\pm.005\,\mathrm{m}$.

2.3. Sirup

Glucose sirup (see Appendix B Sirup) of 43° Baumé[1] is used for the experiments and studies presented in this work. A number of measurements are taken to investigate the physical properties of this sirup. Precise knowledge of these values is crucial for correct model parametrisation and will allow a scaling analysis (see 2.8 Scaling) later on.

In this work the viscosity, density, thermal expansion and thermal diffusivity are investigated and will be discussed in the following sections. For reference, a summary of the results is available in Table 2.2:

$\rho =$	$[1427 \pm 16]\,\mathrm{kg\,m^{-3}}$	2.3.1 Density
$\eta =$	$[154 \pm 13] \cdot 10^6\,(T/^\circ\mathrm{C})^{-4.47\pm0.02}\,\mathrm{Pa\,s}$	2.3.4 Viscosity
$\alpha =$	$\Big([1.56 \pm 0.24]\,T/^\circ\mathrm{C} + [315.67 \pm 13.32]\Big) \cdot 10^{-6}\mathrm{K}^{-1}$	2.3.2 Thermal expansion
$\kappa =$	$1.15 \cdot 10^{-7}\mathrm{m}^2/\mathrm{s}$	2.3.3 Thermal diffusivity

Table 2.2.: Results of the sirup parameter measurements

Experience suggests that the sirup's properties are time- and sample-depended, so it seems prudent to test independent batches separately and to re-check properties in regular intervals.

[1] Degree Baumé is an obsolete density unit which is still used in the food industry

2.3.1. Density

The density can be easily determined by measuring the mass of a defined volume of sirup. The mass of a flask was measured both sirup-filled and empty. Its volume is temperature-dependent, and is $[200 \pm 0.15]$ ml at $[20 \pm 0.1]$°C. An error of ± 2 ml for the measuring of the fill level of the flask is assumed.
Density is defined as

$$\rho = \frac{m}{V} \tag{2.2}$$

To calculate the density error, the propagation of uncertainty can be employed. To calculated the error s_G for a function $G(x_1, \ldots, x_j)$ where s_{x_j} is the error of x_j the propagated uncertainty can be calculated using

$$s_{\overline{G}} = \sqrt{\sum_{j=1}^{n} \left[\left(\frac{\partial G}{\partial x_j} \right)_{\overline{x}_j}^2 s_{\overline{x}_j}^2 \right]} \tag{2.3}$$

For Equation 2.2 this computes to

$$s_\rho = \frac{1}{V} \sqrt{s_m^2 + \left(\frac{m}{V} \right)^2 s_V^2} \tag{2.4}$$

The results are presented in Table 2.3:

Volume (ml)	Mass of empty flask (g)	Mass of full flask (g)	Density (kg/m^3)
200 ± 2	83 ± 1	368.3 ± 1	1427 ± 16

Table 2.3.: Results of density measurement at $[20 \pm 0.1]$°C. Volume error is estimated. Mass errors are standard deviations from three separate measurements, rounded to the accuracy of the scales. The vendor-supplied value is 1410 kg/m^3 at 40°C.

The density is temperature-dependent which is further explored in the next chapter, where an expression for the density as a function of temperature is derived (Equation 2.8).

2.3.2. Thermal expansion

Thermal expansion increases volume while maintaining mass, thus lowering density and creating buoyancy. It is therefore crucial to correctly determine the thermal expansion of the sirup, which is quantified by the coefficient of expansion (CTE).

Prior studies assumed a temperature-independent CTE in the relevant temperature range (≈30–95°C) (Kühnel, 2011). This assumption warrants further investigation, given that sirup contains water (up to 20wt%) (see Appendix B Sirup), whose CTE is strongly temperature-dependent (Figure 2.7 on page 20).

To study the CTE of sirup, a fairly simple setup can be employed: a thin pipe is attached to a flask which is filled with the test fluid (Figure 2.6 on page 18). The flask is brought to a specific temperature, and the fluid level in the pipe is marked. The flask then is heated to another temperature which causes the fluid to expand and rise in the pipe to a new level; that fluid level

is also marked. The distance between the two marks, combined with the pipe's diameter, can be used to calculate the volume of the mean thermal expansion over this temperature interval.

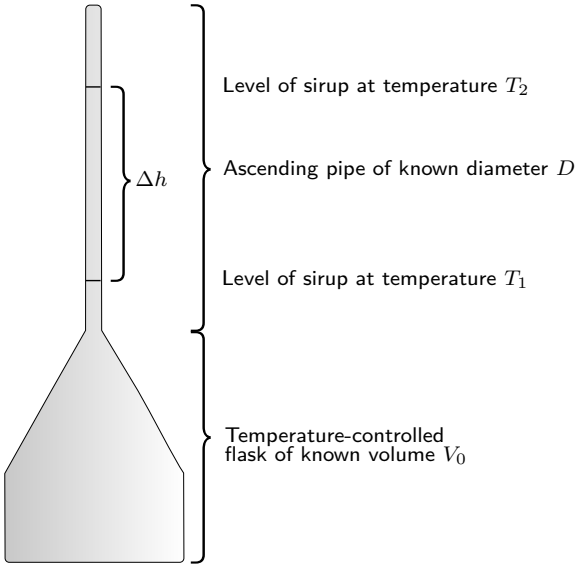

Figure 2.6.: Schematic drawing of the thermal expansion measurement. Liquid is filled in the container and the lower parts of the riser pipe. Different fluid levels, associated with different temperatures, are marked and their distances are measured. The container is submerged in a water bath of precisely known temperature, the pipe is at room temperature.

Even though the riser pipe is not immersed in the water bath, it still can be expected to experience some temperature changes as the flask is heated. As the volume of the riser pipe is negligible (less than 1/30 of the flasks volume), its temperature rise and expansion is neglected. This though will lead to a slight underestimation in the final results[2].

Likewise, the thermal expansion of the flask itself is equally neglected. The flasks expansion can be estimated by taking the volumetric expansion coefficient of (borosilicate) glass ($\alpha_{V,Glass} \approx 9 \cdot 10^{-6}\mathrm{K}^{-1}$ (Mende and Simon, 1975)) times the maximum temperature difference ($\Delta T = 70\mathrm{K}$) and volume ($V \approx 300\mathrm{ml}$). This is about 0.2 ml, compared to 11 ml of the total expansion in this temperature interval. This is equivalent to about 3mm in the riser pipe, compared to its maximum sirup level difference of 137mm, or less then 3%. This will lead to a slight overestimation in the final results.

To control the equipment and establish reasonable precision boundaries, water — whose CTE is well known — is measured as well.

Both water and sirup are measured in intervals of 10°C from 10 to 90 °C (20–90°C for sirup). Before every measurement, the sirup is given 1h to reach the specified temperature (30 min for water, respectively). The results are plotted in comparison to water (Figure 2.7 on page 20) and summarised in Table 2.5 on page 19.

The thermal expansion is calculated using

$$\alpha = \frac{\Delta V}{\Delta T \cdot V_0} = \frac{\pi \cdot D^2 \cdot \Delta h}{4 \cdot \Delta T \cdot V_0} \tag{2.5}$$

[2]Note that this error increases for water, because its lower viscosity leads to some convection in the pipe and heat is exchanged more efficiently with the riser pipe.

with an error (see Equation 2.3) of

$$s_\alpha = \frac{\pi D}{4\Delta T V_0}\sqrt{(2\Delta h s_D)^2 + (D s_{\Delta h})^2 + \left(\frac{D\Delta h}{\Delta T} s_{\Delta T}\right)^2 + \left(\frac{D\Delta h}{V_0} s_{V_0}\right)^2} \tag{2.6}$$

This averages the CTE over the given temperature interval, so the derived value is attributed to the central value of the corresponding temperature interval. This algorithm is implemented in a python program included in the supplemental material (see 5.3 Supplemental material).

#	Temperature range (°C)	Δh (mm)		CTE ($10^{-6}K^{-1}$)	
		sirup	water	sirup	water
1	10–20	–	6	–	121 ± 3
2	20–30	17	11	349 ± 36	221 ± 5
3	30–40	18	19	370 ± 38	382 ± 8
4	40–50	20	23	411 ± 42	462 ± 10
5	50–60	19	31	390 ± 40	623 ± 14
6	60–70	20	19	411 ± 42	382 ± 8
7	70–80	21	24	431 ± 44	483 ± 11
8	80–90	22	33	452 ± 46	664 ± 15

Table 2.4.: Values and results for CTE measurement. The CTE is averaged over the specified temperature range.

These results suggest that the CTE of sirup can quite accurately be described as a linear function of temperature in the given temperature range, or even approximated by a constant, whereas water cannot. The final results are presented in Table 2.5:

#	Coefficient of volumetric thermal expansion α in $10^{-6}\mathrm{K}^{-1}$
1	402 ± 22 or $([1.56 \pm 0.24]T/°\mathrm{C} + [315.67 \pm 13.32])$
Kühnel (2011)	429

Table 2.5.: Result of the thermal expansion measurements. The CTE is temperature-dependent and can be approximated by a linear function and calculated with $\alpha = mT + b$ with an error of $s_\alpha = s_m T + s_b$, where T is the given temperature and presented here as $[m \pm s_m]°\mathrm{C} + [b \pm s_b]$. The CTE can also be estimated by using a constant value for the entire temperature range. Kühnel (2011) did similar experiments and her results are included for comparison.

These results can be combined with the density calculated before to find an expression for density as a function of temperature:

$$\rho = \frac{m}{V} = \frac{m}{V_0 + \Delta V} = \frac{m}{V_0 + \alpha \Delta T V_0} = \frac{\rho_0}{1 + \alpha\,(T - T_0)} \tag{2.7}$$

$$\rho = \frac{1427}{1 + 402 \cdot 10^{-6}\,\frac{1}{°\mathrm{C}}\,(T - 20°\mathrm{C})}\,\frac{\mathrm{kg}}{\mathrm{m}^3} \tag{2.8}$$

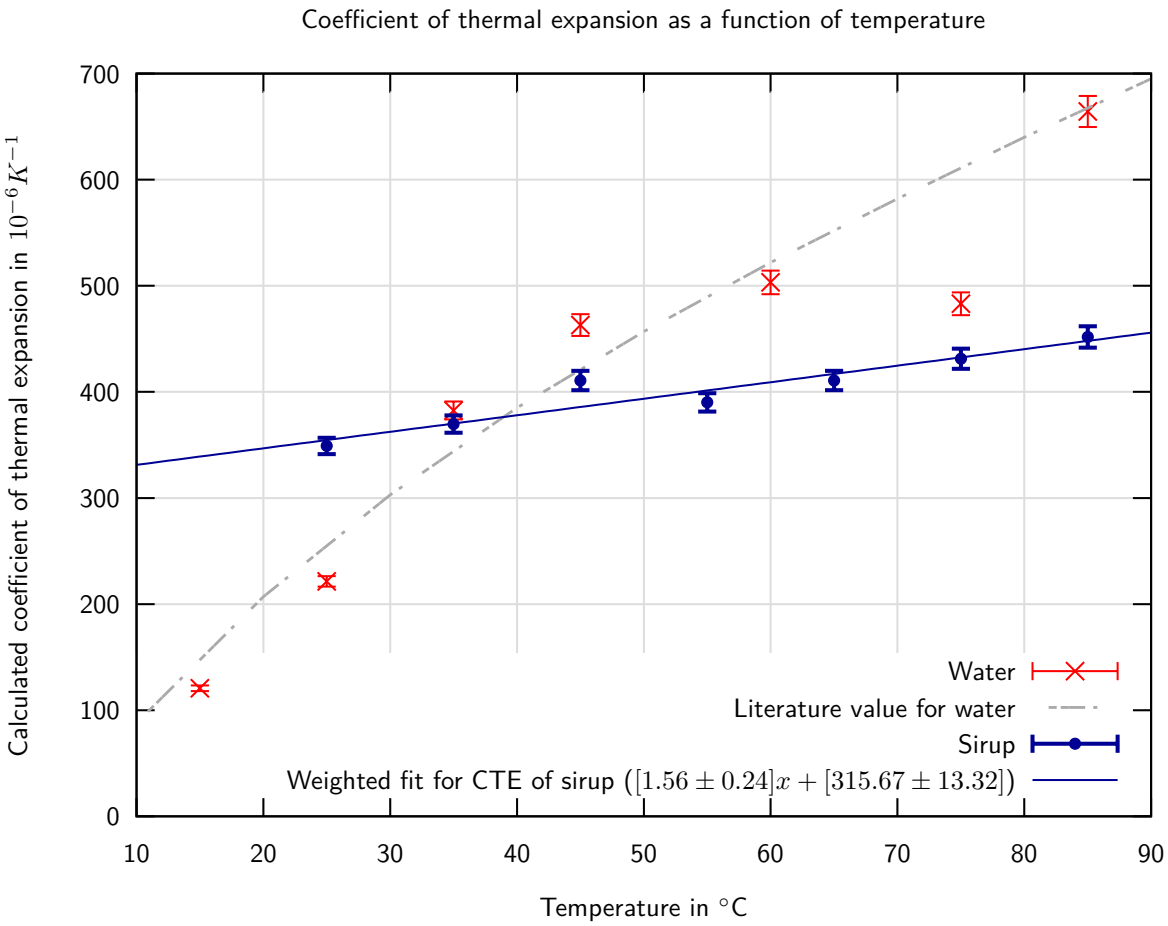

Figure 2.7.: Expansion coefficient of sirup and water as a function of temperature. Each data point represents the averaged value over a ten degree interval. The *measured* value for water at 60°C is an outlier and therefore dropped; thus the interval 50 to 70°C is averaged instead and attributed to the mean value of this interval, 60°C. The CTE of sirup is fitted with a linear function. For comparison, literature values for the expansion coefficient of water (Elert, 2013) are also plotted.
Clearly, the CTE of water is temperature-dependent, but the CTE of sirup can be approximated by a constant value.

with an error of

$$s_\rho = \frac{1}{A^2}\sqrt{A^2 s_{\rho_0}^2 + \rho_0^2 \left(T - T_0\right)^2 s_\alpha^2 + \rho_0^2 \alpha^2 \left(s_T^2 + s_{T_0}^2\right)} \quad \text{where} \quad A = 1 + \alpha \left(T - T_0\right) \tag{2.9}$$

for a non-temperature dependent α. T_0 is the temperature where ρ_0 was measured, so 20°C in this work (see 2.3.1 Density).

2.3.3. Thermal diffusivity

Thermal *conductivity* describes a substance's ability to transport thermal energy through heat conduction. Thermal *diffusivity* describes a substance's ability to conduct thermal energy with respect to its density and heat capacity, and thus its conduction of temperature. Thermal diffusivity can be seen as a kind of thermal inertia.

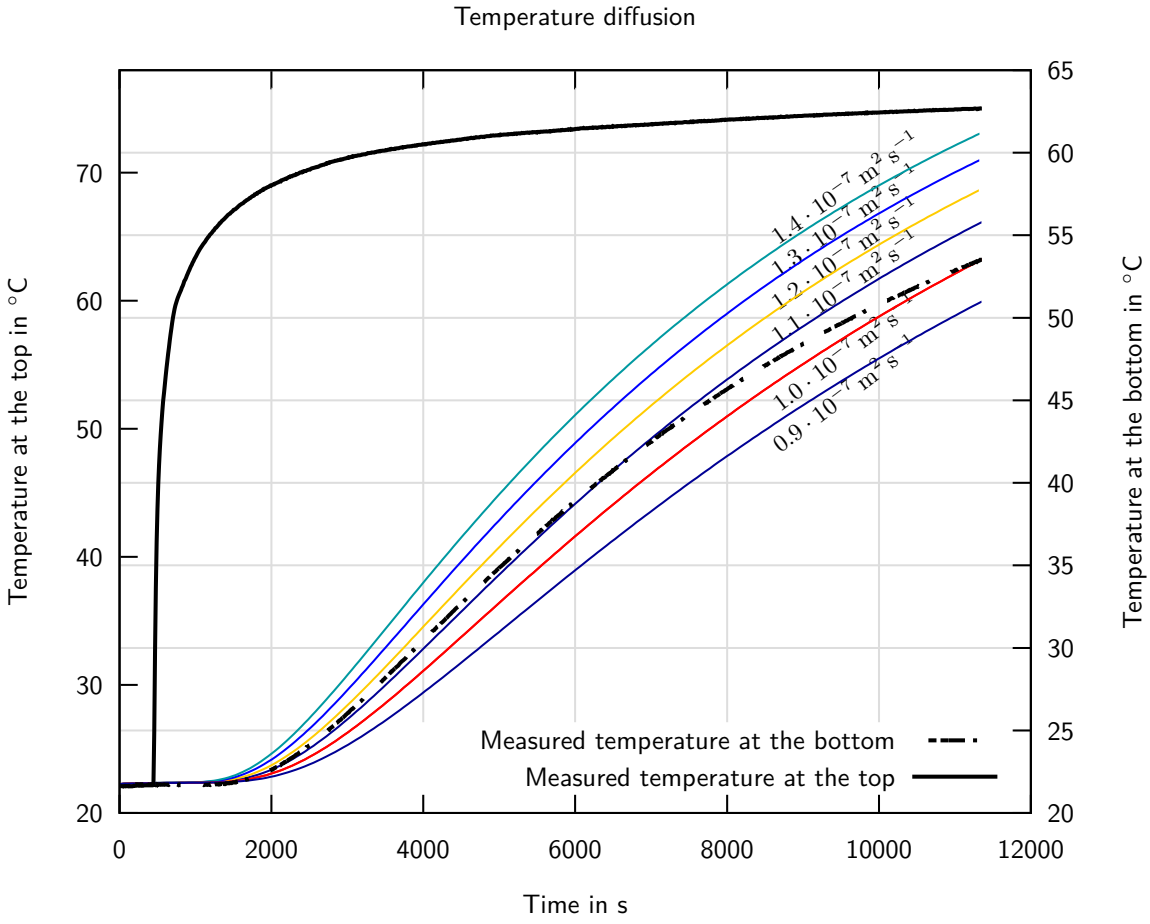

Figure 2.8.: Thermal diffusivity measurement and evaluation. The calibration tank is filled with sirup and its temperature is tracked at the top (thick black solid line) and bottom (thick black dashed line). The sirup is at an isotropic temperature when the top of the tank is heated and brought to a higher temperature. The bottom of the tank receives thermal energy through heat conduction and its temperature rises. The same process is modelled for different values of thermal diffusivity (thin coloured lines). The tank loses heat through the sides which is not modelled in the simulation. That is why in the simulation the bottom temperature converges to the top temperature, and in the measurement to a stable equilibrium slightly below the top temperature.

The thermal diffusivity plays an important role in plume formation. A high thermal diffusivity

favours rapid heat loss from the plume and thus loss of buoyancy. In case of very high thermal diffusivity a plume can get stuck or does not form because the heat is too rapidly dissipated. A low thermal diffusivity allows a plume to maintain its thermal anomaly, and therefore buoyancy, throughout its ascent.

To determine the sirup's thermal diffusivity the temperature diffusion in a small calibration tank (the same as in Figure 2.21) is measured and compared to the results of a computer-aided simulation of the same process. To this end, the calibration tank was brought to an initial isotropic temperature distribution. The experiment begins when the top is suddenly heated. Since the heating occurs at the top of the tank, no convection is induced, and the thermal anomaly is transported downwards only via thermal conduction. At the bottom of the tank a thermocouple is placed, which monitors the arrival and development of the thermal anomaly. During the experiment, the bottom plate temperature is held constant by the second heating bath.

The numerical results are plotted in the same chart as the measurement (Figure 2.8 on page 21) and compared. Due to heat loss present in the experiment, but not in the numerical code, the plots can only be compared up to approximately 40°C. The best fitting curve is $1.15 \cdot 10^{-7}\mathrm{m}^2/\mathrm{s}$. Errors should be expected to be quite high ($\pm 0.1 \cdot 10^{-7}\mathrm{m}^2/\mathrm{s}$). For comparison, water has a thermal diffusivity of $1.43 \cdot 10^{-7}\mathrm{m}^2/\mathrm{s}$.

2.3.4. Viscosity

Viscosity describes a liquid's resistance to applied shear stress. A liquid of low viscosity has a low resistance to stress and will flow easily, while a high viscous fluid is highly resistant to stress and will not flow as easily and quickly under the same amount of applied force. Two concepts are referred to by the term "viscosity": *dynamic* and *kinematic* viscosity. In this work, "viscosity" always refers to *dynamic viscosity*, unless stated otherwise.

Dynamic viscosity or shear viscosity is a term derived by Newton. If two (large) plates are separated by a uniform layer of liquid, the force needed to constantly move one against the other can be calculated using $F = K \cdot A \cdot v/D$, with A being the area of the plates, v the relative velocity, and D the distance between the plates. The factor K is then a measure of the fluids resistance to shearing, which is called dynamic viscosity, or η. The inverse of dynamic viscosity is called fluidity. Dynamic viscosity is typically measured in Pa·s, which is Pascal times seconds.

Kinematic viscosity on the other hand is the dynamic viscosity divided by the fluid's density, mostly used for convenience.

$$\nu = \frac{\eta}{\rho} \tag{2.10}$$

The kinematic viscosity can also be seen as a measure for momentum diffusion in the liquid.

A fluid is said to be *Newtonian* if its viscosity is constant for any given temperature and not dependent on current shear rate, deformation history, etc. (Tritton, 1999). For the purpose of this work, sirup can be assumed to be Newtonian. Non-Newtonian behaviour is investigated further below, but a thorough investigation is beyond of scope of this study.

One should be careful to distinguish viscosity from rheology, as these terms are not generally interchangeable. *Viscosity* describes a fluids resistance to stress and can be easily measured using

a viscometer. *Rheology* describes the flow behaviour of a liquid, which can be time-, stress- and temperature-dependent.

In applications with nearly isotropic Newtonian fluids, the rheology of a liquid is entirely determined by its viscosity, and the viscosity is exclusively dependent on temperature.

Falling Sphere Viscometer

A falling sphere viscometer is an instrument to measure the viscosity of a liquid at a defined temperature. In its simplest form, a falling sphere viscometer is a container filled with the liquid in question, and a sphere of metal or other dense material which sinks in the fluid. Using the Stoke's equation, the terminal velocity of the sphere and the density difference, the dynamic viscosity can be calculated (see below). An improved version of this kind of viscometer is the Höppler style viscometer. It uses a tube with a slightly larger radius than the sphere, filled with a fluid sample. The tube is enclosed in a water jacket which is connected to an external circulating bath. The assembly is angled at about 80° to the horizontal. The assembly can be easily turned upside down, and thus the measurement can be repeated (Figure 2.9).

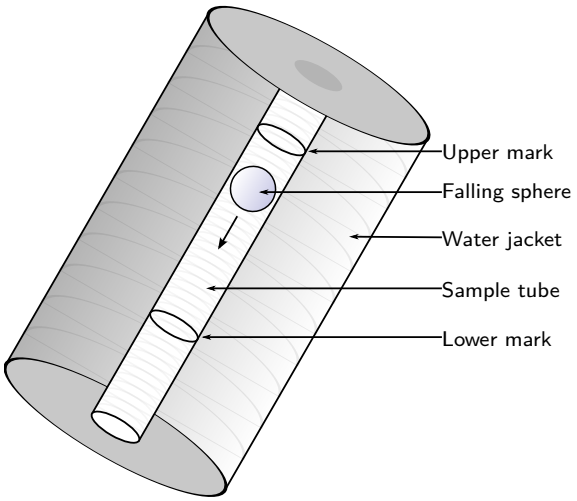

Figure 2.9.: Working principle of the Höppler style viscometer. A tube ("Sample Tube") is filled with a fluid of unknown viscosity. The sample tube is set within a water jacket that is connected to a precisely temperature controlled water bath. A small dense sphere is left to migrate downwards through the liquid, driven by gravitation. The whole assembly is inclined at 80° to horizontal to reduce unwanted horizontal movement of the sphere. The sphere's travel time between two marks is measured and used to calculate the viscosity by comparison to the travel time in a liquid of known viscosity. This only works for laminar flows with $\mathrm{Re} \ll 1$ (see 2.8 Scaling), so travel times <30s should be avoided as per the viscometers manual.

In this experiment a falling sphere viscometer made by Haake (B 90 155, DIN 53015) is used. It employs a sphere made of steel with a diameter of $[15.0 \pm 0.05]$ mm, a mass of $[13.78 \pm 0.015]$ g and a density of $[7799.8 \pm 22.5]\,\mathrm{kg/m^3}$ (own measurements).

Once the sphere has reached its terminal velocity, its movement can be described by a steady state equation, with its gravitational force balancing buoyancy and drag forces.

$$F_{\mathsf{Gravitation}} = F_{\mathsf{Boyancy}} + F_{\mathsf{Drag}} \tag{2.11}$$

The buoyancy is equal to the gravitational force of the liquid the sphere displaces (Archimedes'

principle). The drag force can be calculated using Stoke's law:

$$F_{\mathsf{Drag}} = F_{\mathsf{Stokes}} = 6\pi\eta r v \tag{2.12}$$

$$F_{\mathsf{Boyancy}} = V g \rho_{\mathsf{Liquid}} \sin\alpha \tag{2.13}$$

$$F_{\mathsf{Gravitation}} = V g \rho_{\mathsf{Sphere}} \sin\alpha \tag{2.14}$$

with V being the volume of the sphere, r its radius, g the local gravitational acceleration, α the inclination of the assembly and v the terminal velocity of the sphere. This can be transformed into:

$$F_{\mathsf{Stokes}} = F_{\mathsf{Gravitation}} - F_{\mathsf{Boyancy}} \tag{2.15}$$

and solved for η, using L for the distance of the marks:

$$6\pi\eta r v = V g \rho_{\mathsf{Sphere}} \sin\alpha - V g \rho_{\mathsf{Liquid}} \sin\alpha \tag{2.16}$$

$$\eta = \frac{Vg}{6\pi r L} \sin\alpha \left(\rho_{\mathsf{Sphere}} - \rho_{\mathsf{Liquid}}\right) t \quad \text{with } v = \frac{L}{t} \tag{2.17}$$

$$\eta = K \left(\rho_{\mathsf{Sphere}} - \rho_{\mathsf{Liquid}}\right) t \quad \text{with } K = \frac{Vg}{6\pi r L} \sin\alpha \tag{2.18}$$

With η being the viscosity and ρ the density, K is a constant coefficient for this test setup and is independent of the fluid and measurement. This coefficient is called Sphere (or Ball) Factor. Using this, only the densities and the corresponding travel time of the sphere for a new liquid (or temperature) have to be measured. The equation can be transformed into:

$$K = \frac{\eta}{\left(\rho_{\mathsf{Sphere}} - \rho_{\mathsf{Fluid}}\right) t} \tag{2.19}$$

to calculate the sphere factor using a liquid of known density and viscosity. With this method the factors α, V, g, r and L are eliminated and the simplified Equation 2.18 can be used to calculate viscosity.

In order to determine the sphere factor K, a standard fluid (Brookfield B200) is used. Its density is measured in the same way as before (see 2.3.1 Density) and is calculated to be $\rho_{\mathsf{B200}} = 865 \pm 10.0\,\mathrm{Kg/m^3}$. Its viscosity is known to be $0.2033\,\mathrm{Pa\,s} \pm 1\% = [0.2033 \pm 0.002]\ \mathrm{Pa\,s}$. The travel time is measured to be $[26.61 \pm 0.13]\,\mathrm{s}$. The sphere factor K therefore is $[1.10 \pm 0.01]\,10^{-6}\mathrm{Pa\,m^3/kg}$.

The equation can be further simplified by using a constant value for the density difference, but in this work the more precise Equation 2.8 is used for every viscosity calculation.

For each temperature step, the sphere's travel time between the marks (Figure 2.9 on page 23) is measured for both directions. There was little difference between the directions, still the measurements were averaged. At higher temperatures ($> 80°\mathrm{C}$) an air bubble got trapped and compromised some measurements — these were discarded (results see Table 2.6 on page 25).

The viscosity in this temperature range (35–95°C) can be approximated with a simple function of the form $m \cdot x^n$. Note however, that this functional relationship is not to imply a physical law, but merely a fit to the specific values obtained by the measurements. Hence, this fitted function is unsuited for extrapolation. The relationship between viscosity and temperature is much more

difficult, and cannot be expressed using a simple function (Evans and Morriss, 1988). So the final results for the viscosity in the range from 35°C to 95°C are (Figure 2.10 on page 26):

$$\eta = [154 \pm 13] \cdot 10^6 \, (T/^\circ\mathrm{C})^{-4.47 \pm 0.02} \, \mathrm{Pa\,s} \quad \text{with T = Temperature in °C} \tag{2.20}$$

Temperature (°C)	Traveltime (s)	Viscosity (Pa s)	Viscosity (Pa s) from Datasheet
20	–	–	ca. 100
30	–	–	ca. 30
34.65	2742 ± 25	19.26 ± 0.31	–
39.5	1588 ± 7	11.16 ± 0.14	ca. 9 (at 40°C)
44.4	968 ± 6	6.80 ± 0.09	–
49.3	615 ± 7	4.32 ± 0.07	ca. 4 (at 50°C)
54.25	401.9 ± 0.61	2.826 ± 0.034	–
59.2	271.7 ± 0.69	1.911 ± 0.023	–
64.15	188.8 ± 0.85	1.328 ± 0.017	–
69.1	134.6 ± 0.94	0.947 ± 0.013	–
74.0	98.5 ± 1.0	0.693 ± 0.011	–
79.0	72.2 ± 0.72	0.5082 ± 0.0079	–
84.0	54.9 ± 0.48	0.3865 ± 0.0057	–
89.0	42.6 ± 0.16	0.3000 ± 0.0038	–
93.9	33.4 ± 0.18	0.2352 ± 0.0031	–

Table 2.6.: Falling Sphere Viscometer: traveltime and viscosity as a function of temperature with averaged values for each temperature. Vendor supplied values are included as a reference (see Appendix B Sirup). Since the manufacturer's data is not very precise, slight deviations from these values are to be expected. Temperatures are picked from thermocouple temperature measurements in the water jacket (see Figure 2.9); the error can be expected to be less than ±0.1°C.

Rheometer

Rheology is the study of the flow behaviour of liquids, solids and gases. For the applications in this work, the temperature-dependence of viscosity is most interesting, but there might be a dependency on shear rate as well, which both will be the subject of this study. Additionally, this is a chance to verify the results obtained by the viscometer (see 2.3.4 Falling Sphere Viscometer).

I use a R/S+ Rheotec Searle principal rheometer (Figure 2.11 on page 27). Because this instrument is new, its temperature reliability (how well the rheometer measures the test fluid's temperature) will be determined. To get a general idea of how reliable the results from this instrument are, fluids of known viscosity are measured as well.

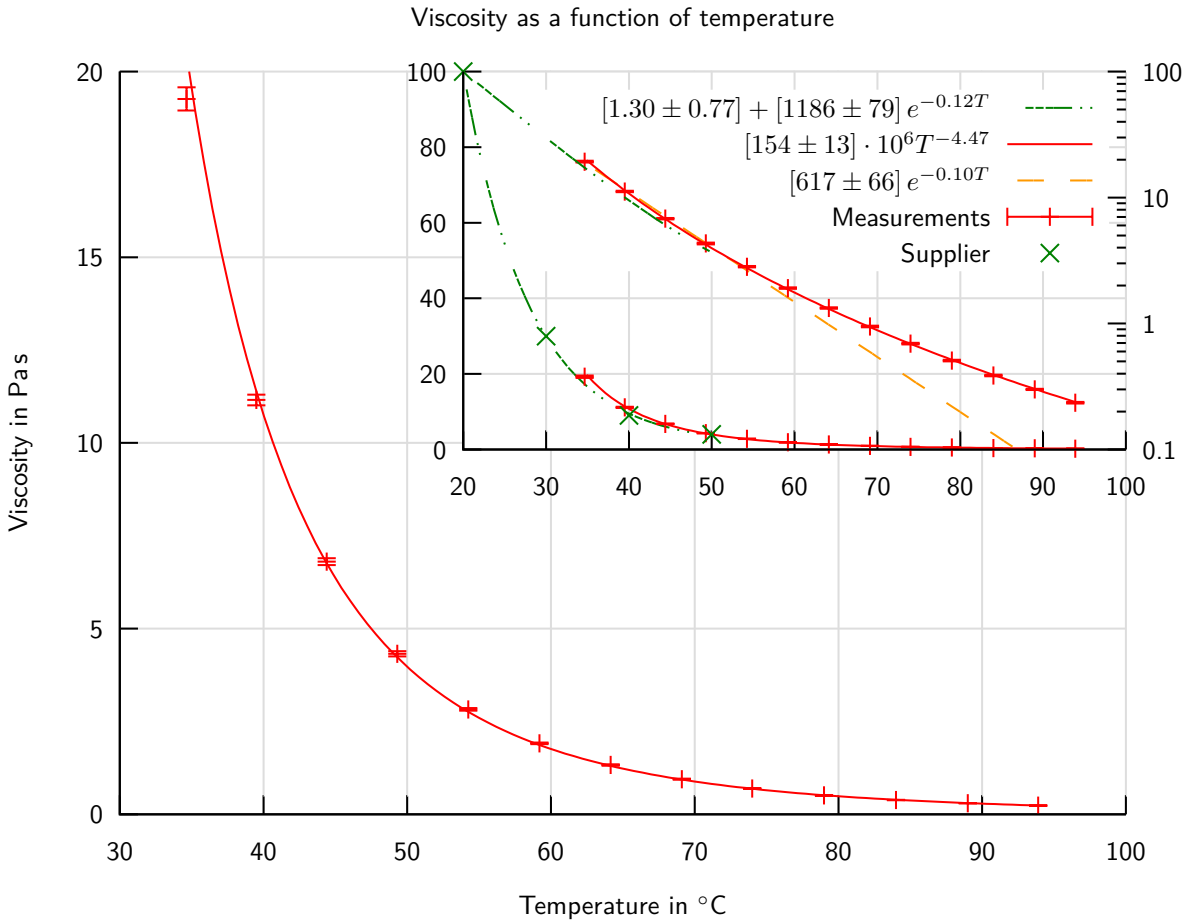

Figure 2.10.: Viscosity as a function of temperature. The inset graph shows the viscosity's dependency on temperature compared to the manufacturer's values. The manufacturer's values are fitted using a exponential function ($a \cdot e^{x \cdot c}$), the measurements using a potential function ($a \cdot b^{x \cdot c}$). Both are plotted to a standard linear scale (on the left, left hand plots) as well as a logarithmic scale (on the right, right hand plots). Note that it may be deceiving to directly compare the fitted functions of the manufacturer's values to the fitted function of the measurements. Both are interpolations using the best fitting function, not any valid physical model. As such, they should not be extrapolated. For reference, the measured values are interpolated using an exponential function, which is typically used for this purpose. Also note that sirup can be expected to have some variation between charges. Experience also suggest that it is not stable over long time periods. Depending on storage conditions, its properties can change quite drastically, exceeding factor 2 for viscosity.

The rheometer can use arbitrary shear rate or shear stress profiles. Different profiles are used in this study for different purposes: "pyramid", "saw" and "constant" (Figure 2.13 on page 28).

The *pyramid* scheme is convenient for simple and quick viscosity measurements over a shear stress range. The *saw* profile repeats the pyramid profile and is especially useful to measure the

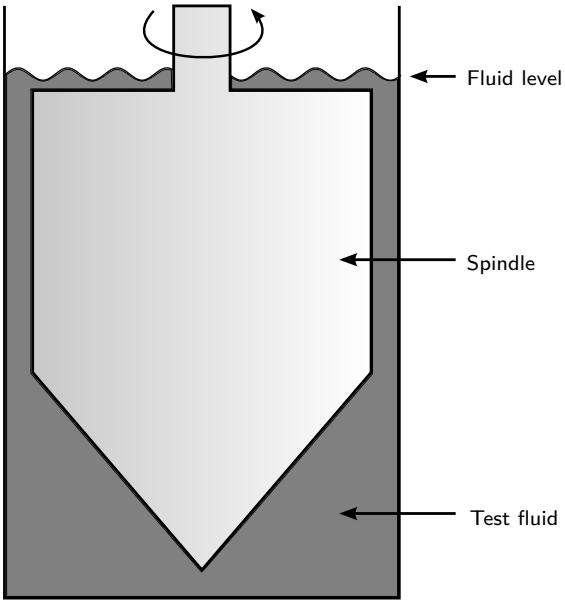

Figure 2.11.: Working principle of a Searle-type rheometer. A cylinder ("coaxial cylinder spindle") is rotated in a larger cylinder ("chamber"). The chamber is enclosed in a water jacket which is connected to a temperature-controlled water bath. The resulting gap is filled with a sample of the test fluid (also see Figure 2.12). The rheometer can be set to use a fixed shear stress and measure the shear rate, or vice versa. There is a limit for the torque and circumferential velocity range for the motor, thus different sizes for the inner and outer cylinder ("systems") are available and are used for different viscosity ranges (see *Systems & profiles*).

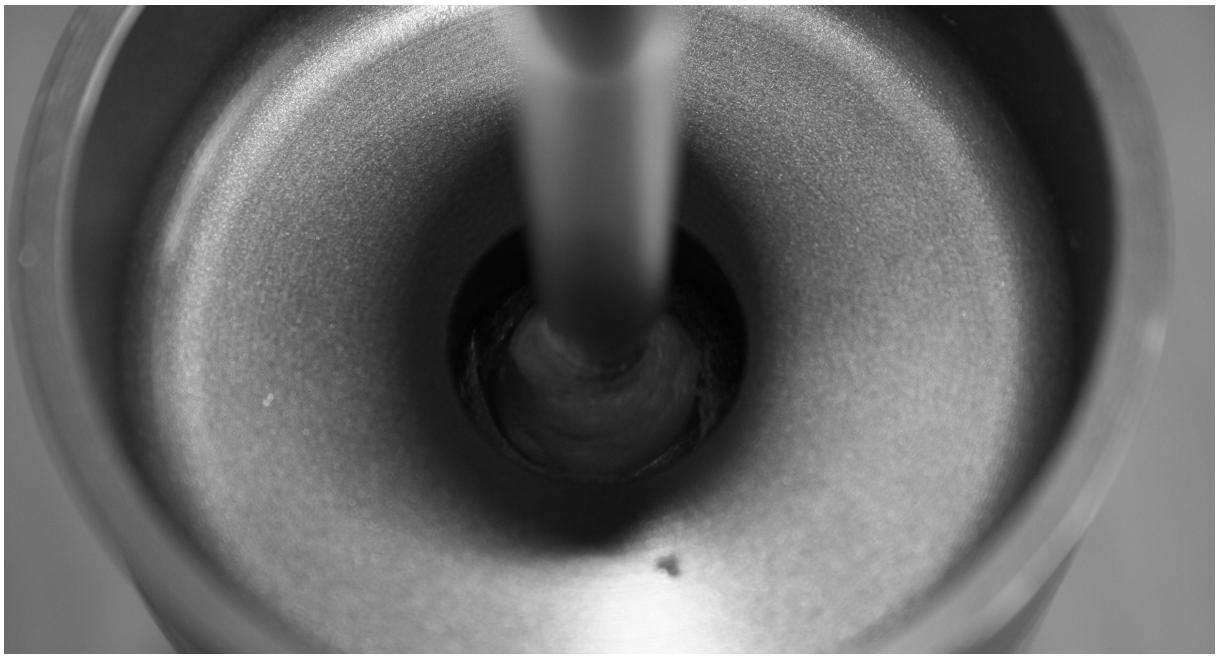

Figure 2.12.: Close-up photograph of the test chamber (centre) of a Searle-type rheometer with test fluid and spindle. The spindle is connected to a motor (not pictured) that measures the required force to rotate the spindle in the fluid. The test chamber is enclosed in a metal water jacket, which is connected to a thermally controlled bath (not pictured).

effects of time-dependent viscosity. The maximum torque the instrument can deliver is limited, and thus the pyramid and saw profile cannot always be completed. The *constant* profile—set to an acceptable shear stress or rate—is an alternative in these cases.

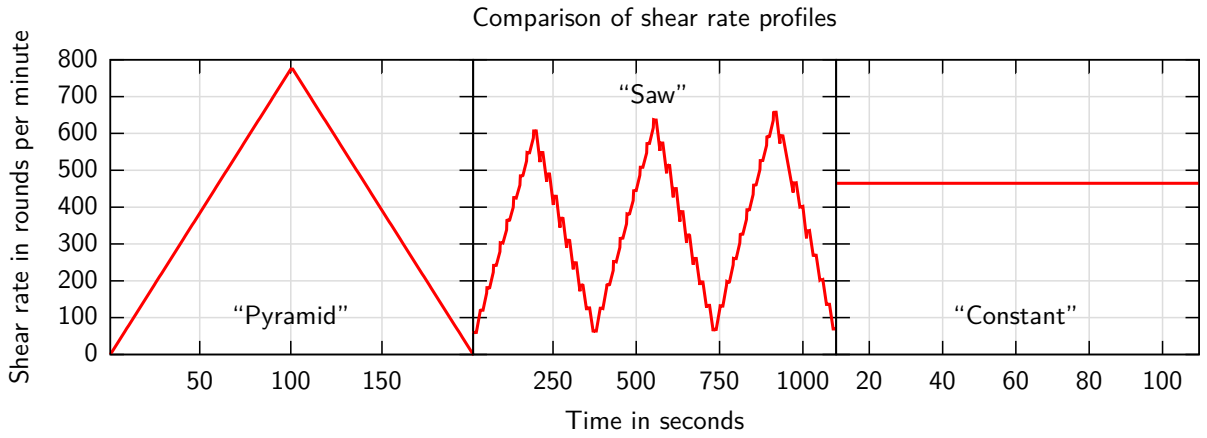

Figure 2.13.: Illustration of different shear rate profiles. These schemes are used for all viscosity-to-shear-rate measurements, but the actual ranges can vary for different liquids to accommodate the max- and minimum torque of the instrument.

Temperature reliability & correction.

To determine the reliability of the rheometer's own temperature measurement a thermocouple is placed inside the test chamber next to the probe. A rheometer measurement is started (with 0 rpm) while the thermocouple temperature is monitored. The simultaneous measurements are plotted (Figure 2.14 on page 29). The temperature measured by the thermocouple (green values) is slightly lower than the rheometer measurement (red values), and the deviation is temperature-dependent — the higher the background temperature, the bigger the temperature gap.

In the temperature range 40–90°C, the temperature should be corrected as

$$T_{\text{real}} = T_{\text{apparent}} - 0.02 \cdot (T_{\text{apparent}} - 25°\text{C}) \tag{2.21}$$

$$= 0.98 \cdot T_{\text{apparent}} + 0.5°\text{C} \tag{2.22}$$

Systems & profiles.

The rheometer used in these experiments features the ability to use different sample chamber / spindle combinations, which are suitable for different viscosity ranges. These are referred to as "systems" in this work. Three systems as well as three calibration fluids (viscosity error: ±1%), are available:

system	shear rate	max shear stress
CC14	1–1291 s^{-1}	6500 Pa
CC25	1–1291 s^{-1}	1140 Pa
CC45	1–2184 s^{-1}	287 Pa

fluid	viscosity at 20°C
B200	0.2033 Pa
B2000	2.013 Pa
B10200	9.834 Pa

Table 2.7.: Overview of available rheology measuring systems and test fluids.

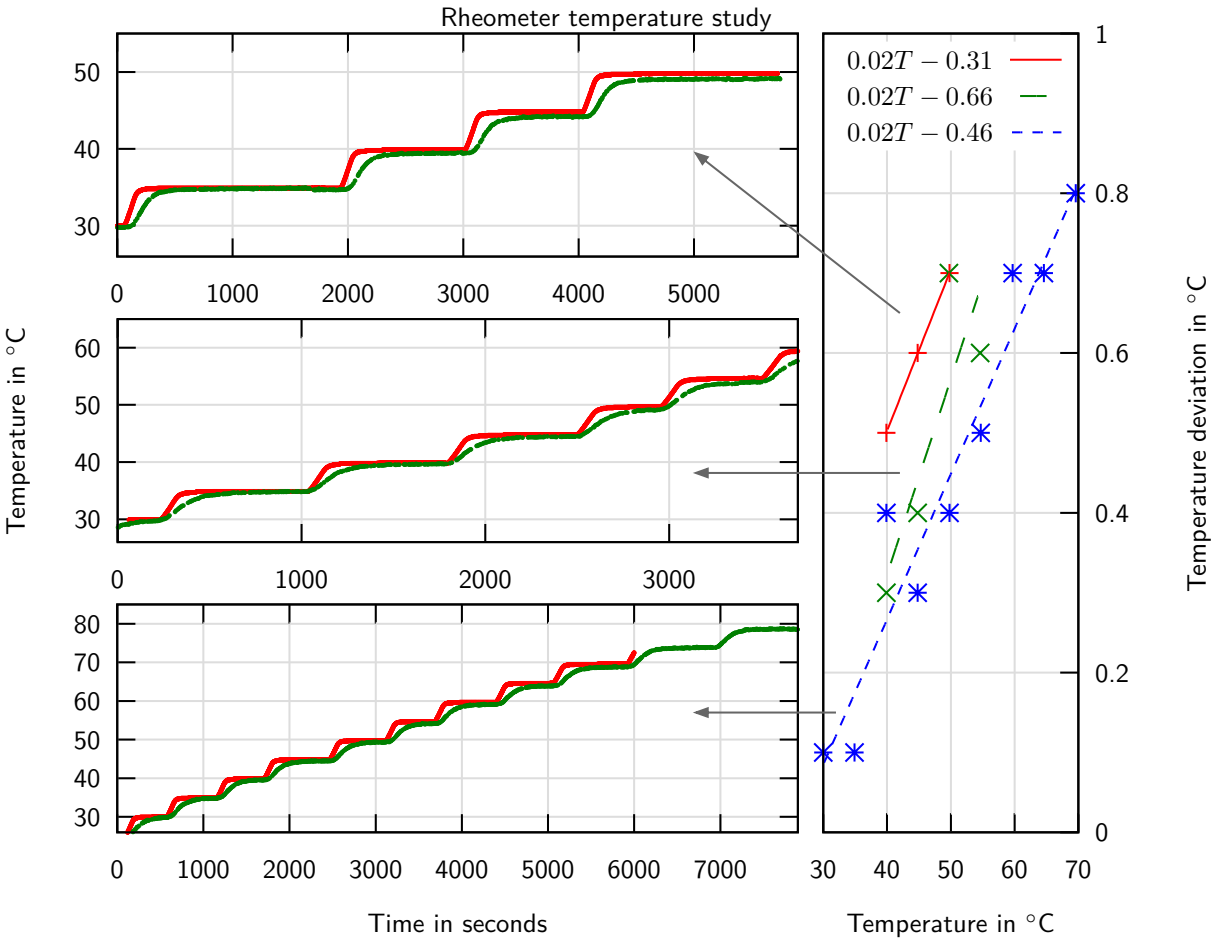

Figure 2.14.: Temperature deviation of in-situ thermocouple measurement compared to the rheometer's displayed temperature as a function of background temperature. Red values refer to the rheometer's own temperature measurements in the water jacket, green to the thermocouple embedded in the sample chamber. The water jacket's temperature is almost always higher, and picks up temperature changes more quickly than the sample itself. On the left are three independent measurements of temperature as a function of time (note the different ranges on both axes). On the right are the minimal temperature differences between rheometer and thermocouple for each temperature step of the three measurements with a linear fit. The legend contains the fit parameters that can be used as a correction function for future measurements. The arrows indicate which deviations are taken from which measurement. Please note that only system CC14 was tested. While the correction factor should be very similar for the other systems (CC25, CC45; see Systems & profiles), it still should be determined individually. It also only applies after a prolonged waiting period (>30 minutes) and at room temperature.

All systems are tested using the three calibration fluids and the different profiles. Results are summarised in Figure 2.15.

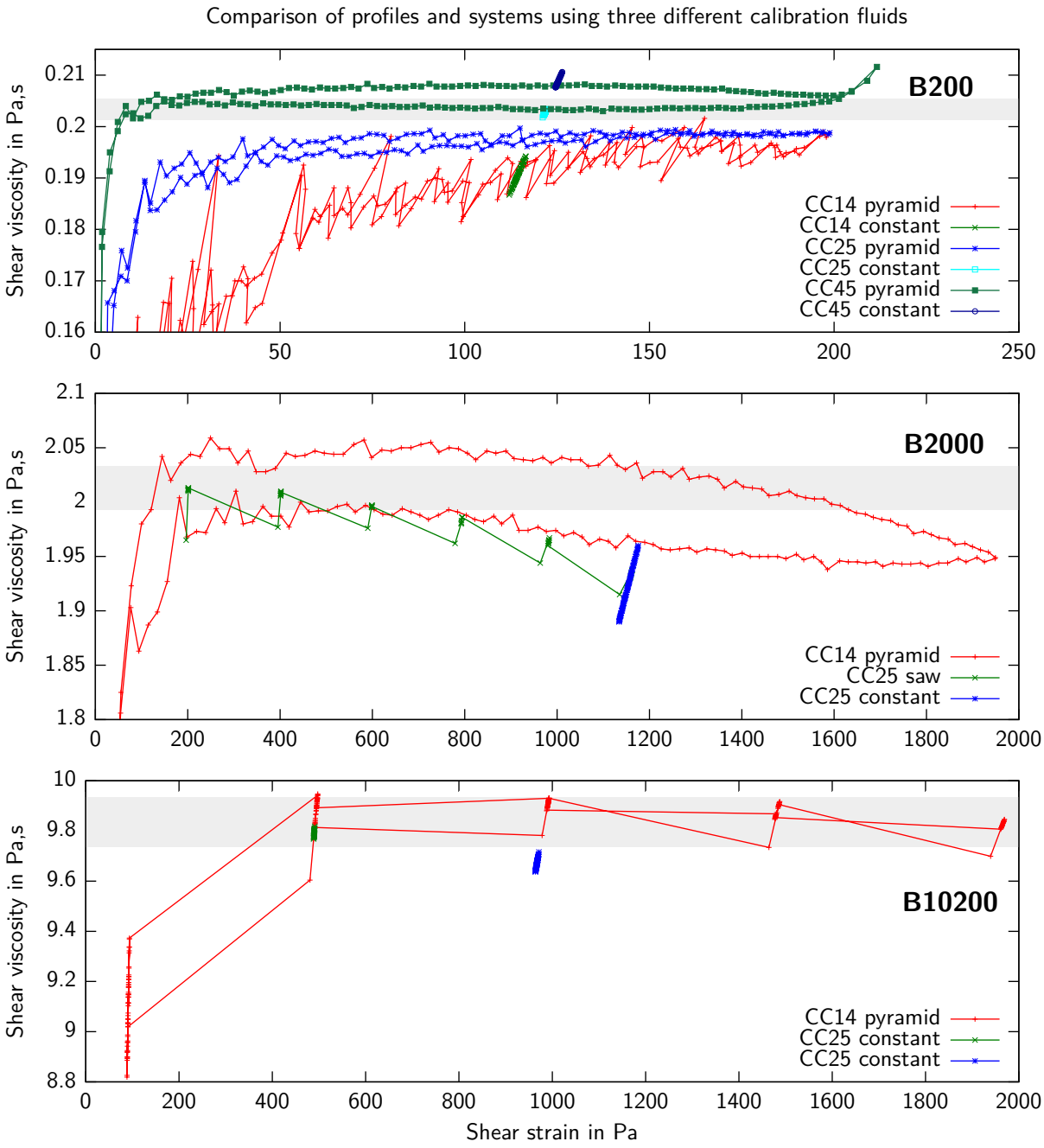

Figure 2.15.: Comparison of different rheometer systems. The topmost plot is for the calibration fluid B200, the middle one for B2000 and the bottom one for B10200. The respective viscosity and relative error are shown as grey bars (value ±1%). Ideally, the recorded values should lie within the gray areas. Different profiles where used, all of which show slight rheopextic behaviour. The term "constant" refers to a constant shear rate. As the viscosity changes, the shear strain (which is plotted here) has to be adjusted to maintain a constant shear rate, thus the "constant" profiles are not necessarily constant here.

Viscosity dependence on shear rate.

As with most real liquids, the sirup's viscosity can be expected to be dependent on the shear rate (and not be ideally Newtonian). To estimate this effect on the flow in the experiments it would be interesting to know the range of shear rate to be expected in the experiments, and therefore the associated viscosity change. An upper estimate of the magnitude of this effect will help to determine its impact on the experiments.

Plumes are investigate in the main experiments (see 3 Experiments) and the highest shear rates can be assumed to be in the region of the highest velocity differences, which would be the plume's tail.

The tail can be roughly described to be similar to a pipe. The shear rate at the inner surface of a pipe is

$$\dot{\gamma} = \frac{8v}{d} \tag{2.23}$$

with γ being the shear, $\dot{\gamma}$ the rate of shear change, v the fluids velocity and d the pipes diameter. Shear rate is related to shear stress—if Newtonian behaviour is assumed—through

$$\tau = \eta\dot{\gamma} \tag{2.24}$$

with τ as the shear stress, and η the viscosity. Thus, the shear stress in a pipe is

$$\tau = \eta\frac{8v}{d} \tag{2.25}$$

The plume's tail usually has a radius greater than 2 cm. The highest velocity that is observed is well under 0.1 m/s. The highest viscosity is 20 Pa s. Hence, the estimate for the shear rate is considerably less than $4000\,\mathrm{s}^{-1}$.

To determine the shear rate dependency the "saw" profile (Figure 2.13 on page 28) is used for several temperatures and every rheometer system (Figure 2.11 on page 27). A typical measurement is plotted in Figure 2.16:

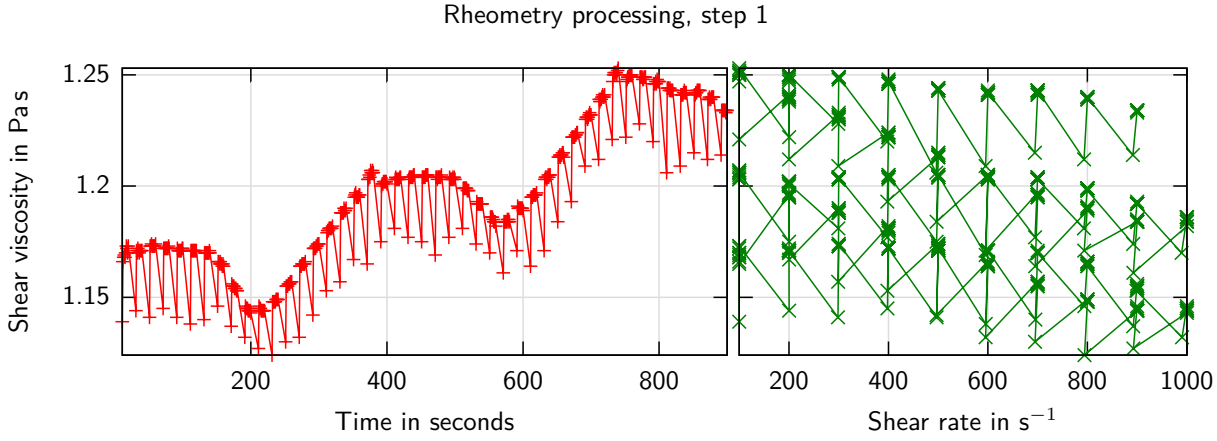

Figure 2.16.: Viscosity measurements of sirup at 75°C using system CC25 and the "saw" profile. On the left side shear viscosity is plotted as a function of time and on the right side the shear viscosity (same axis and scale as left hand plot) as a function of shear rate.

With the "saw" profile, the rheometer takes several measurements at each shear rate step. The first data point is always lower on the shear rate scale (=slower rotation) than it should be, and yields an unexpected low shear viscosity value. It can reasonably well be assumed that this behaviour is a measurement artefact, so these data points are discarded as outliers. The results are fitted with a linear function (Figure 2.17).

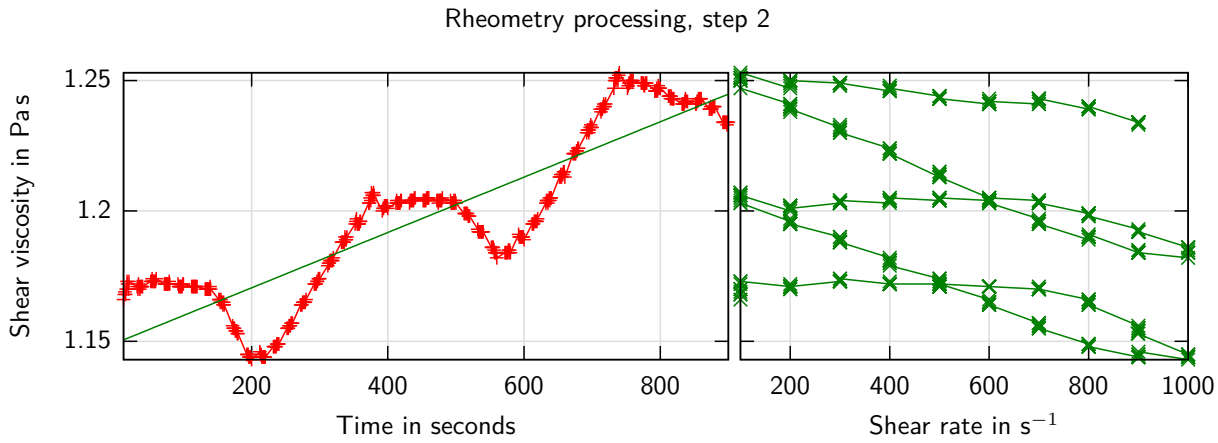

Figure 2.17.: Same as Figure 2.16 but with the first data point from every time step removed and a linear fit added to the time series.

There is an obvious time-dependent trend in the data, which could be a symptom of a number of effects. Sirup could be slightly rheopexic (a liquid whose shear viscosity increases with time under shear) or there might be a time-dependent systematic error in the experimental setup (e.g. water evaporation)[3].

In any case, the time dependency can be removed easily by subtracting the linear fit function from each data point (Figure 2.18 on page 33):

[3]Possible time dependency might warrant further investigation, but is not included in this work

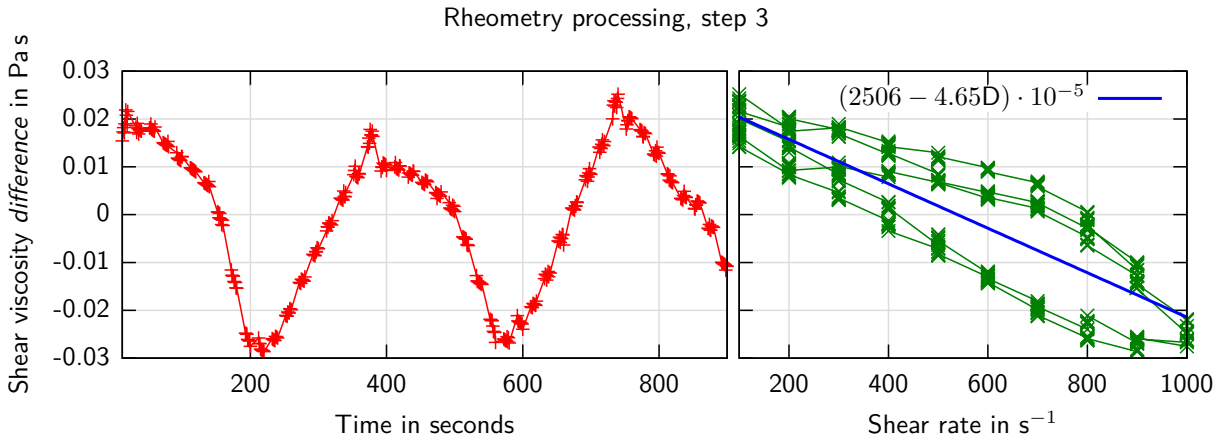

Figure 2.18.: Same as Figure 2.17 but corrected for time dependence. The shear viscosity's dependency on shear rate can be fitted linearly as $(2506 - 4.65D) \cdot 10^{-5}$, with D as the shear rate.

The final data at this temperature and with this system reveals very slight shear thinning behaviour (viscosity decreases when shear forces increase) which is further illustrated in Figure 2.19:

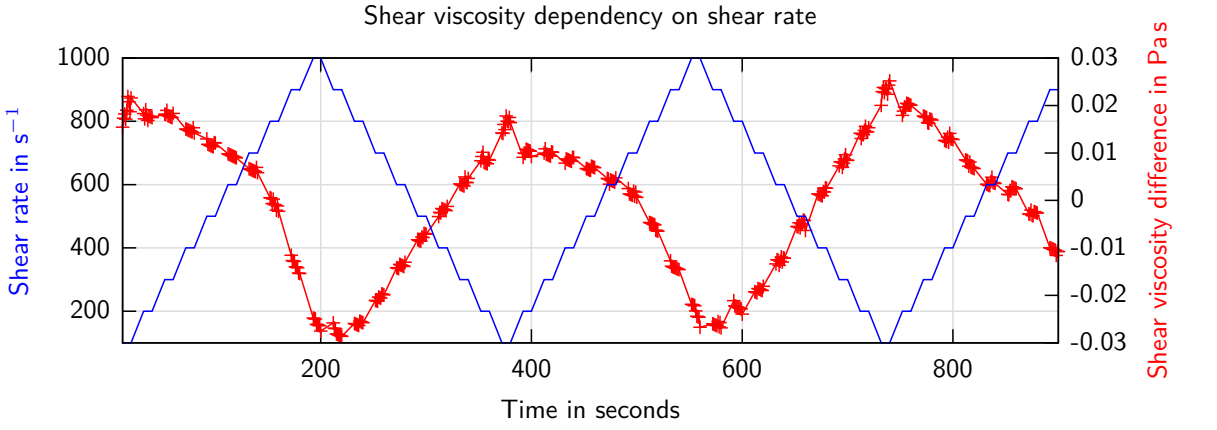

Figure 2.19.: Shear rate and corresponding shear viscosity change. Shear viscosity is clearly correlated with shear rate. The correlation function is determined in Figure 2.18.

This process is repeated for every system at different temperatures and the results are summarised in Table 2.8. Shear thinning is much too low to be of any effect in the main measurements[4], so no correction will be needed.

[4]Max. effect of shear thinning: $20 \cdot 10^{-5}\text{Pas}^2 \times 4000\text{s}^{-1} \approx 0.8\text{Pa s}$

	at 55°C ($\mathrm{Pa\,s^2}$)	at 65°C ($\mathrm{Pa\,s^2}$)	at 75°C ($\mathrm{Pa\,s^2}$)	at 85°C ($\mathrm{Pa\,s^2}$)	at 95°C ($\mathrm{Pa\,s^2}$)
CC14	$-19.33 \cdot 10^{-5}$	$-6.29 \cdot 10^{-5}$	$-0.48 \cdot 10^{-5}$	$-4.61 \cdot 10^{-5}$	$+5.80 \cdot 10^{-5}$
CC25	$-7.58 \cdot 10^{-5}$	$-4.19 \cdot 10^{-5}$	$-3.90 \cdot 10^{-5}$	$-3.92 \cdot 10^{-5}$	$-0.24 \cdot 10^{-5}$

Table 2.8.: Summary of the viscosity-to-shear-rate measurements. Each value represents the sirup's shear rate dependency on viscosity at a specific temperature in $[\eta/\mathrm{D}] = \mathrm{Pa\,s/s^{-1}} = \mathrm{Pa\,s^2}$. The sirup is too viscous for the system CC45 to complete the "saw" profile, thus the results from that system are discarded.

Temperature dependency.

The temperature dependency is measured using the "saw" profile ("constant" for CC45) and is summarised in Figure 2.20.

Unfortunately, the results obtained from the rheometer are contradictory to the results from the falling ball viscometer (see 2.3.4 Falling Sphere Viscometer). Since the falling ball viscometer is simpler, less error-prone, and has proven to give reproducible measurements, the results from this experiment are discarded and the results from the falling ball viscometer are used for the calculations and models in this work.

2.4. Particles

For PIV to work particles are needed that are embedded in the fluid to produce discernible patterns. These particles need to be good reflectors and neutrally buoyant in the liquid. Four types of particles are available: Hollow Glass Spheres (HGS), Silver-Coated Glass Spheres (S-HGS), Glass Particles (Glass Powder), and Vestosint. All these materials are commonly in use in PIV applications.

The particles used must not introduce an additional rising or sinking velocity that would interfere with the measured velocity by PIV. The sinking (or rising) velocity can be estimated using Stoke's Law if the particles are assumed to be of spherical shape and the flow around them to be laminar. Their relative velocity is then equal to their terminal velocity.

The terminal or **settling velocity** is the stable velocity a particle reaches when sinking or rising due to its density (see 2.3.4 Falling Sphere Viscometer) and can be derived from Equation 2.16 (on page 24):

$$v_T = \frac{2}{9} \frac{(\rho_p - \rho_f)}{\eta} g\, R^2 \tag{2.26}$$

To derive the upper estimate, only the lowest values for the sirup's density (ρ_f) and viscosity (η) are needed to calculate the terminal velocity for all available particles (Table 2.9 on page 35):

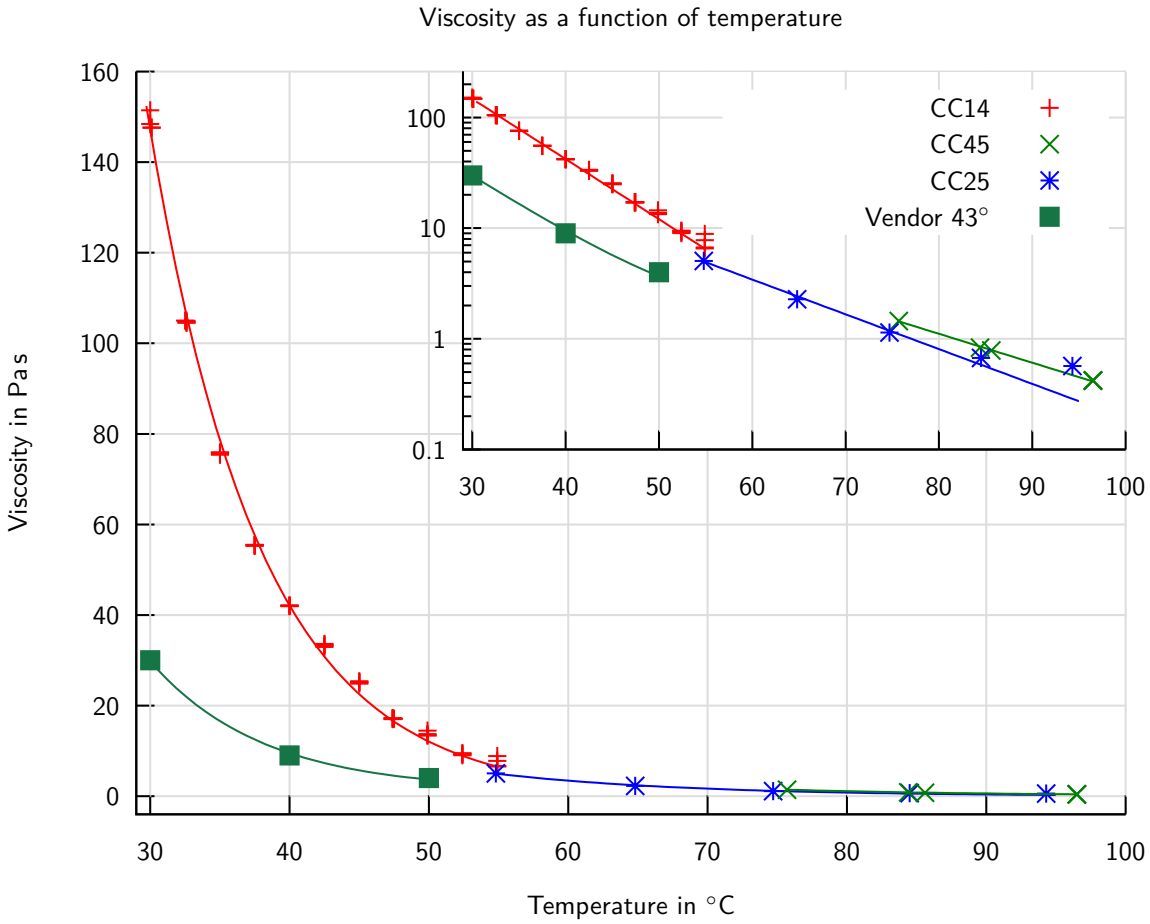

Figure 2.20.: Results from the rheometer experiments. The viscosity of sirup is measured as a function of temperature. The inset graph displays the same data, but on a logarithmic scale. Values are interpolated using functions of the form $a \cdot e^{b \cdot x}$.

Name	Diameter	Density $(\frac{kg}{m^3})$	v_T $(\frac{mm}{s})$
Hollow Glass Spheres (HGS)	10 µm	1100	$< -8.2 \cdot 10^{-6}$
Silver-Coated Glass Spheres (S-HGS)	10 µm	1400	$< -0.3 \cdot 10^{-6}$
Glass Powder	< 30 µm	2500	$< +0.26 \cdot 10^{-3}$
VESTOSINT 1111	32 . . . 250 µm	1016	$< -8.8 \cdot 10^{-3}$
Air bubbles	1 . . . 0.1 mm	≈ 0	$< -1.5 \cdot 10^{-(1...3)}$

Table 2.9.: Available particles. Particles with positive values for v_T sink, those with negative values rise up. For PIV, values of less then 0.02 mm/s are acceptable. Values for Vestosint (Evonik Industries, 2013), HGS and S-HGS (Dantec Dynamics, 2013) are taken from the manufactures catalogue, the value for Glass Powder is estimated from a very similar product (Schott AG, 2013). Air bubbles tend to get trapped in the sirup. Smaller bubbles remain static within the experiments and can even help with PIV, but larger ones affect the flow field negatively. Air bubble size roughly estimated.

These calculations confirm that the relative particle velocities are negligible over the time frame of a single measurement — even for glass power less than 1 mm during the entire experiment[5]. For the experiments silver coated hollow glass spheres (S-HGS) are used, because they also produce the brightest reflections.

2.5. Thermochromatic Liquid Crystals (TLC)

Liquid crystals are materials which present both crystalline as well as fluid properties within a certain temperature range. They become crystalline below, and fluids above that range and can be called a new state of matter in between crystalline solid and isotropic liquid.

Liquid crystals occur both naturally as well as man-made. They have interesting optical properties, some can be changed by magnetic or electrical fields. Liquid crystals are widely used in liquid crystal displays (LCDs).

Thermochromatic Liquid Crystals (TLCs) are liquid crystals with temperature-dependent optical properties. Specifically for this application, TLCs with temperature-dependent colour for contactless temperature measurements are used. Since TLCs can be tailored to specific temperature/colour ranges with comparably high resolution ($\pm 1°C$), they are widely employed in both commercial as well as scientific applications that cannot be satisfied using traditional thermometers. In science, TLCs are used where thermometers are either not practical or even disruptive. Since I aim to examine flow fields, I want to use in-situ contactless measurements which do not disrupt the flow or introduce unwanted thermal bridges.

The colour of temperature-dependent liquid crystals usually undergoes a change through the visible light spectrum, starting at red for lower, passing green and ending at blue for higher temperatures. Both the specific temperature — at which this change occurs — as well as the bandwidth are determined by the manufacturer.

Unshielded TLCs are not particularly stable and react with surrounding chemicals, particularly solvents and oxygen. To prevent degradation, TLCs are enclosed ("coated") in microcapsules, which dramatically increases their durability.

The TLCs in this study are dispensed in a water-based slurry, which is mixed with the sirup and are assumed to remain neutrally buoyant for the duration of one experiment. TLC concentration is at levels of 10^{-3} vol%. It is unlikely that they will significantly alter the physical properties of the sirup at this concentration.

To measure the TLC's properties, a small calibration tank is filled with TLC enriched sirup, heated from above and cooled from below. This way thermal convection is suppressed and a stable temperature gradient from top to bottom is established. For the purpose of this experiment, a perfect linear gradient can be assumed, which should be true to a good approximation.

The tank then is illuminated from the side with a laser (using a sheet optic to broaden the beam to a vertical plane) and photographed from the front (Figure 2.21 on page 37), similar to the main experiment. The temperature is monitored using two thermocouples at the top and bottom.

[5]The particles can however "escape" from the experimental fluid and accumulate at the top (or bottom) over a relatively long time (a month) which explains the apparent loss of particle density observed in the measurements.

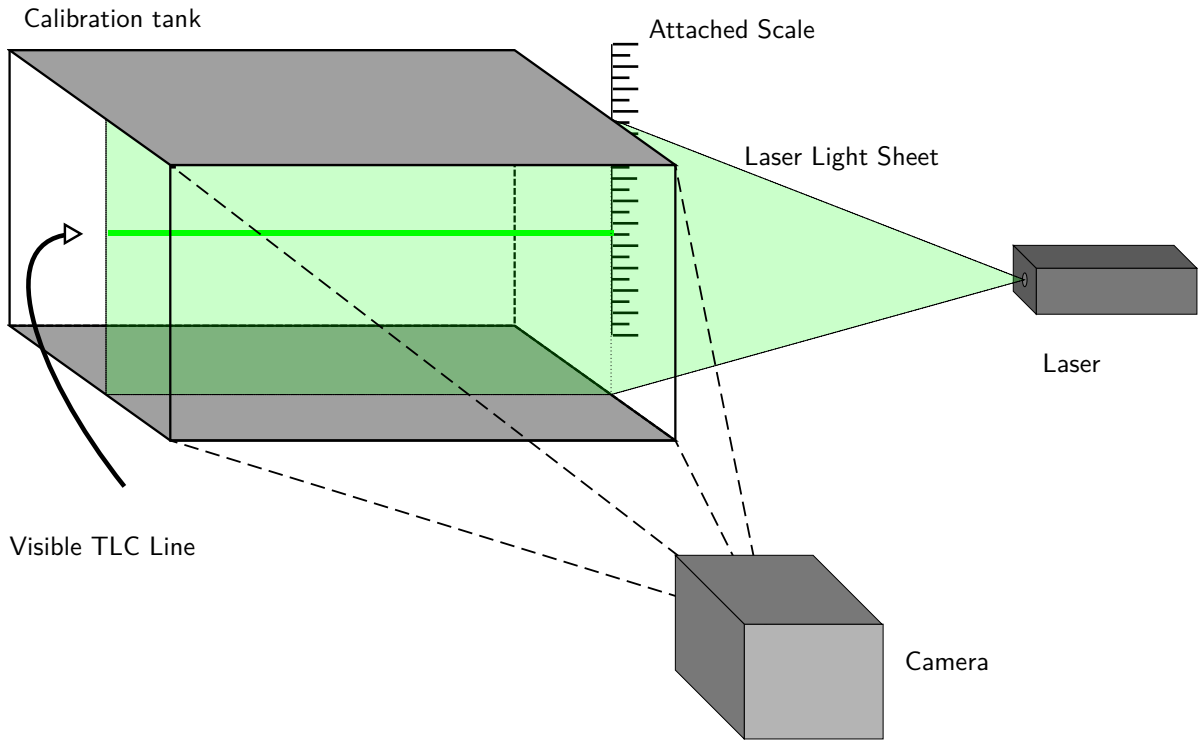

Figure 2.21.: Sketch of the TLC calibration setup. A stable linear temperature gradient is established in the calibration tank, which is illuminated by a laser from the side and photographed from the front. A scale is attached parallel to the light sheet. Two thermocouples are mounted inside the tank at the top and bottom, horizontally centered.

Because the TLCs colour is linked to their temperature and because of the temperature gradient from top to bottom within the tank, at some point the TLCs colour matches the laser lights colour (e.g. red and green) and a plane in the tank becomes reflective. The temperature is uniform on each horizontal plane within the tank, and the laser light sheet is vertical. The result of this is a bright visible line which links temperature to TLC visibility. The temperature gradient is known to be linear between two points of fixed temperature, so the TLC's associated temperature is known if the line's position is measured.

Two properties are important for this study in particular: the concentration of TLCs in sirup that fits best the final experiments and the temperature at which they are visible.

2.5.1. Concentration

Finding the right concentration of liquid crystals is somewhat difficult. On the one hand, a high concentration yields a strong TLC reflection, on the other hand TLCs that are not in the visible temperature range appear grey and thus dim and diffuse light. A high TLC concentration dims TLC lines and reduces contrast, while at the same time occluding the rest of the image which can

hamper particle velocimetry. This dimming also leads to a brightness gradient in the direction of the laser (Figure 2.22). A low concentration on the other hand leads to a weak signal which is difficult or even impossible to measure.

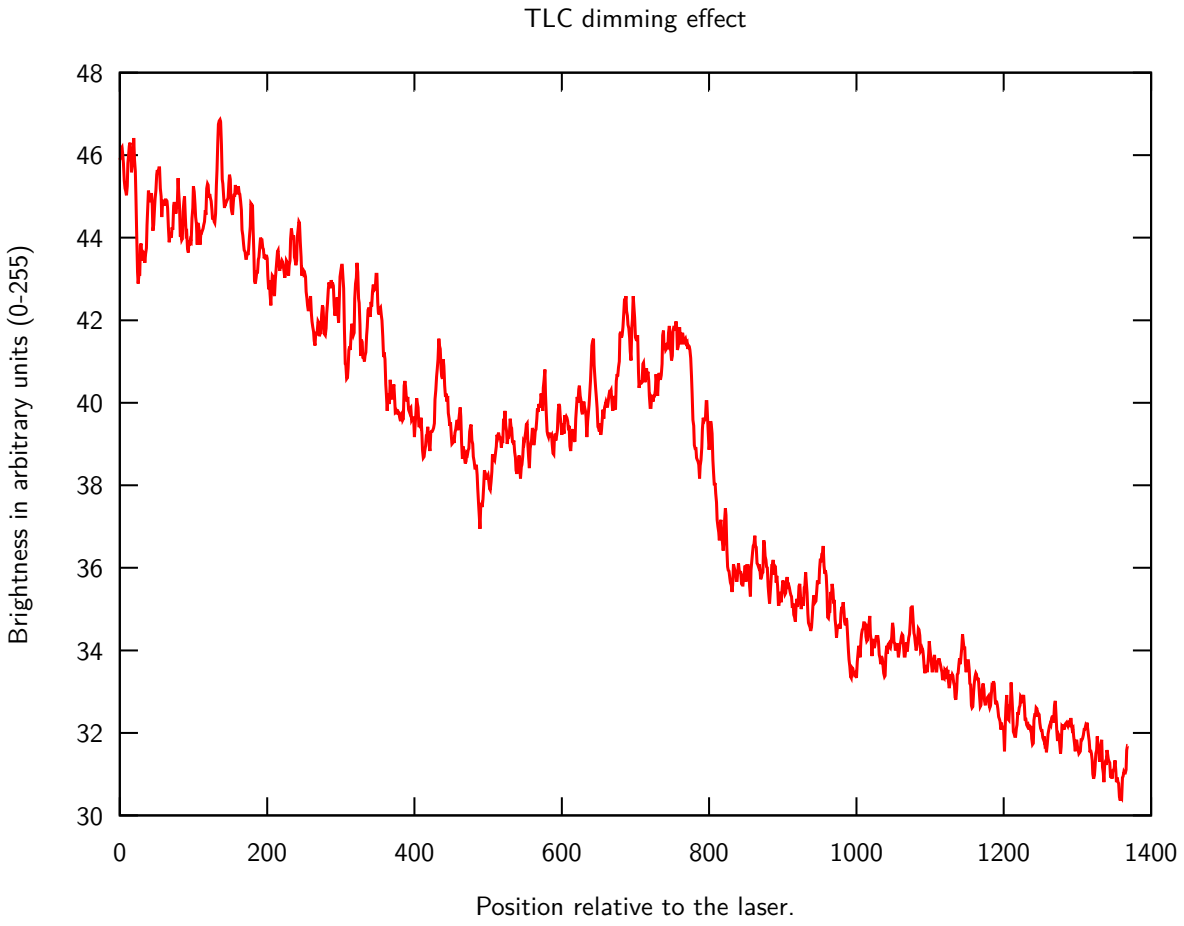

Figure 2.22.: Effect of TLC dimming: Averaged laser brightness plotted against distance to laser. Laser light enters the tank from the left and is continuously dimmed.

Combining three different kinds of TLCs exacerbates these effects: dimming is additive, while the signal is not. While different TLCs take part in the dimming, they are only visible in different temperature regimes.

Because contrast depends on a range of parameters that depend on the specific setup, the definite answer for TLCs concentration cannot be given here, but good concentrations are in the order of 10^{-2} vol% (Kühnel, 2011).

A good and objective method to determine the best concentration in regard to contrast might be to plot the averaged brightness and to compare the TLC peak height compared to the background brightness (almost identical to the calibration technique discussed previously (see

2.5.2 Calibration)).

Another study was done to compare different concentrations directly: the calibration tank was divided into three compartments and filled with water. Compared to sirup, water is very easy to handle because it mixes quickly and uniformly with the TLC slurry. A process which can take an hour of mixing sirup manually and days of purely convection-driven mixing takes seconds in water. The calibration setup is the same (Figure 2.23).

While this method is somewhat informative for finding a reasonable start value, this measurement cannot be adequately used to compare different concentration levels because all three compartments receive different illumination levels. The laser is considerably dimmed through the TLCs and compartment walls, so the compartment farthest from the laser is considerably darker. It should be noted that water is, while easy to handle, not an ideal substitute for the sirup. Sirup—unlike water—is not clear and darkens even more in the course of the experiments. Because of this, these types of measurements are not directly transferable.

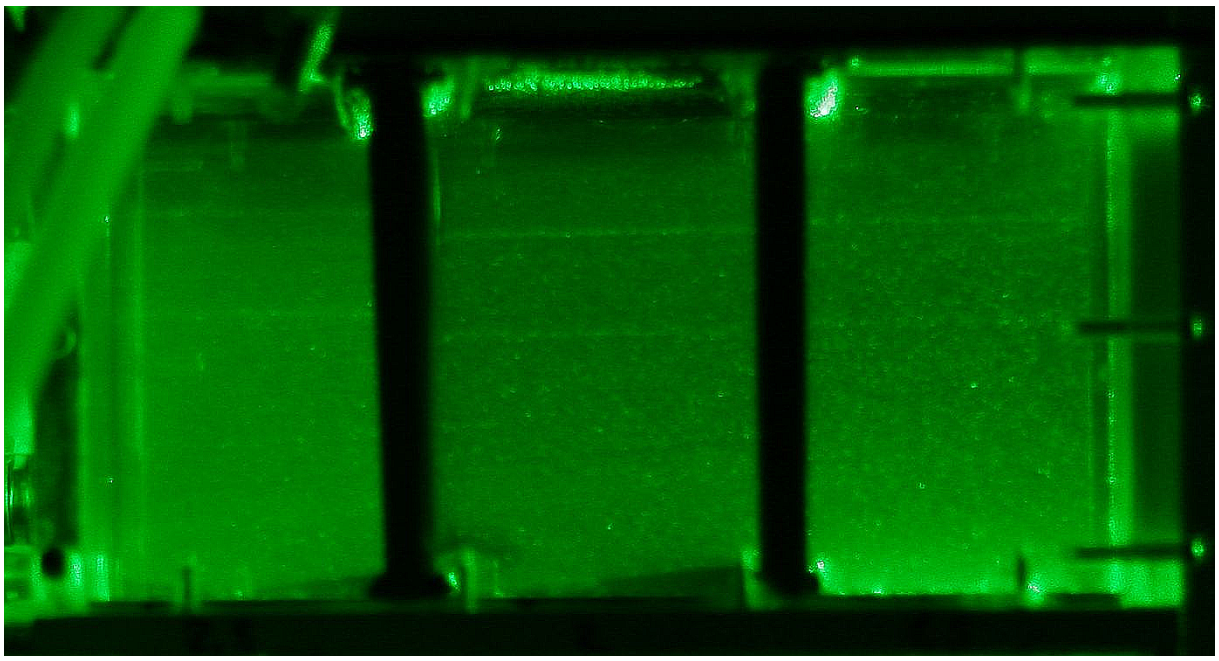

Figure 2.23.: Comparison of different TLC concentrations

Because I was unable to get good TLC readings, and because TLCs have an adverse effect on PIV analysis, no TLCs were used in the main experiments in this work. The results from this chapter will however be valuable in future studies.

2.5.2. Calibration

The thermochromic liquid crystals must be calibrated to ensure that the visible lines in the experiments can be properly attributed to correct temperature later on. TLC NSL40/R54C2W is used because it is suited best for for the application in this work.

A calibration was done for both the red and green laser (see 2.6 Laser); unfortunately, the red laser is not sufficiently visible to be measurable or useful in the final experiments, so it was left out.

To accurately measure the position of the TLC line, a photograph was taken, enhanced, and digitally interpreted. Since the TLC line should be considerably brighter than the surrounding layers, it will show up as a peak in a vertical brightness plot.

A thin white line is drawn onto the image to mark the upper boundary. The TLC position is then easily measured by the distance between the two highest brightness peaks in the plot (artificial white line and TLC line).

This can be done automatically for every vertical slice and then averaged by the computer. The peak distance is evaluated using a simple Matlab/Octave script[6] which is available in the supplemental material (see 5.3 Supplemental material).

The TLC's visible bandwidth for this laser is defined by the width of the second peak (Limare et al., 2008). Programmatically measuring the peak's width is no trivial task, so the peak's width is estimated from the graph (Figure 2.24 on page 41)[7].

Using the same technique, a conversion factor between mm and px can be derived: The attached scale is pictured onto the same image as the measurements (Figure 2.25 on page 42). Then the distance between the cm marks can be determined by plotting the brightness. A peak detection algorithm is used to measure the lowest dips, which corresponds to the cm marks. The distance between the cm marks are 135px, 134px, 134px (averaged over two marks) and 135px which yields an average of $[13.45 \pm 0.06]\,\frac{px}{mm}$.

To measure the temperature, two thermocouples, one at the top and one at the bottom of the tank, are installed. The resulting specific temperature for this laser and TLC then is calculated by

$$T_{\text{Specific}} = T_{\text{Top}} - \frac{\Delta H_{\text{Top}}}{CH}\left(T_{\text{Top}} - T_{\text{Bottom}}\right) \tag{2.27}$$

where dH_{Top} equals the distance from the top to the TLC line, H the total height of the test chamber ($[100 \pm 1]\,mm$), C the conversion factor between px and mm, and T_{Top} and T_{Bottom} the temperature at the top and bottom of the tank.

Uncertainty is calculated using the propagation of uncertainty (see Equation 2.3) which in this case gives (using $\Delta T = T_{\mathsf{Top}} - T_{\mathsf{Bottom}}$):

$$s_{\overline{G}} = \sqrt{\left(1 - \frac{\Delta H}{CH}\right)^2 s_{T_{\text{T}}}^2 + \left(\frac{\Delta H}{CH}\right)^2 s_{T_{\text{B}}}^2 + \left(\frac{\Delta T}{CH}\right)^2 s_{\Delta H}^2 + \left(\frac{\Delta H}{CH^2}\Delta T\right)^2 s_H^2 + \left(\frac{\Delta H}{C^2 H}\Delta T\right)^2 s_C^2} \tag{2.28}$$

T is measured using thermocouples (see 2.2 Thermocouples) and averaged over several minutes, H is known (100 mm with an estimated error of ± 1 mm) and ΔH_{Top} can be measured by image processing (see above). For different measurements T_{Top} and T_{Bottom} are adjusted.

[6] Which uses PEAKDET 3.4.05 by Eli Billauer

[7] First, another method was tried: a scale was taped to the side of the tank and the visible TLC line was then extrapolated onto the scale and the value read. This method suffered from light defraction at the passage from sirup to glass to air and its low scale resolution (in the order of mm). Other setups, including submerging the scale, were also tried, but did not work well in practice.

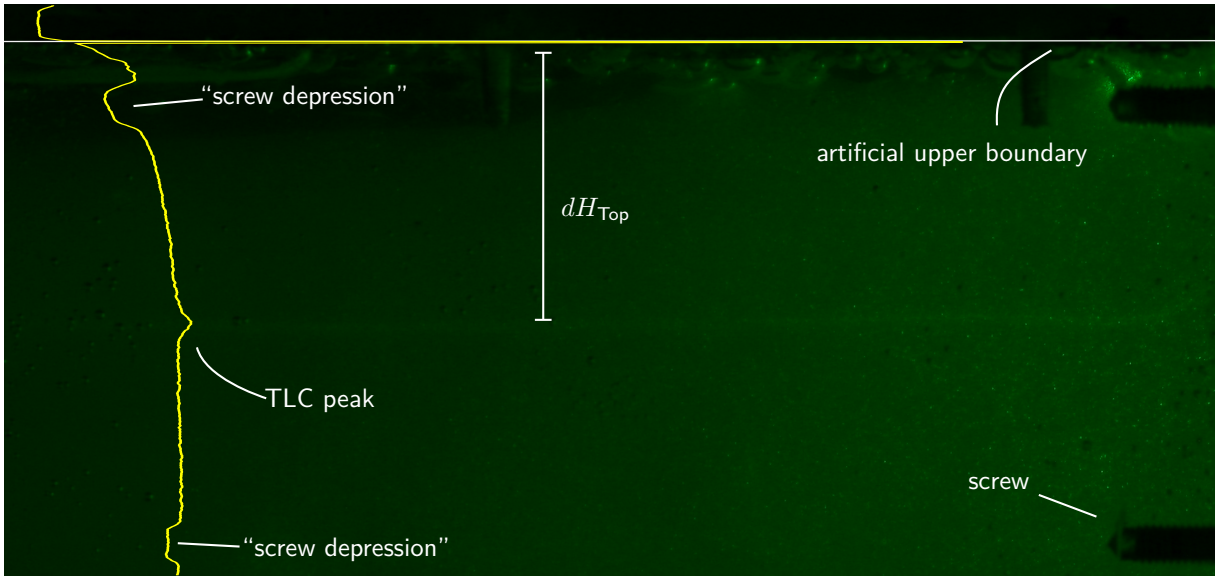

Figure 2.24.: Photograph of TLC calibration measurement overlayed with colour brightness plot. Because the green laser is used, only the green colour channel of the image is used. The brightness then is a number between 0 and 255 for every pixel. Higher is brighter. The brightness is averaged for every horizontal line of the image, and plotted against height. Because TLCs reflect light only in a specific temperature, the layer of sirup with the temperature corresponding to the same colour as the laser is brighter than the surrounding material. This results in a peak in the brightness plot ("TLC peak"). The "screw depression" is a localised decrease in average brightness due to screws in the tank on the right side. To measure the TLC line's distance to the top of the tank (ΔH_{Top}) a white line ("artifical upper boundary") is drawn onto the images, resulting in a sharp peak in the brightness plot.

As already noted, the calculated specific temperature is a result of the combination of properties of the laser used in this experiment as well as the TLC's. Both the TLCs and the lasers age and not necessarily remain stable over time and thus the results are not generally applicable to other experiments and setups.

The results are presented in Table 2.10. The deviation in the repeated measurements is unsatisfactory and indicates systematic errors in the setup that are still unexplained.

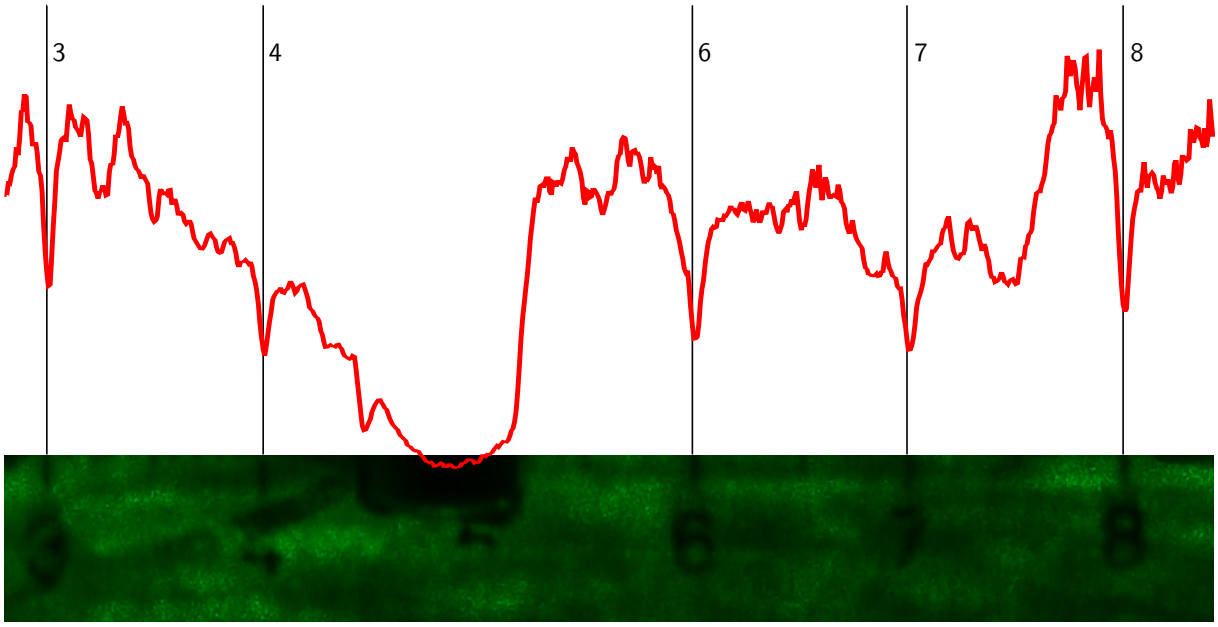

Figure 2.25.: Illustration of px to mm ratio measurement. The scale is cropped from the images and its brightness is plotted. A peak detection algorithm is used to measure the lowest dips, which corresponds to the cm marks. Mark "5" is obstructed by a screw.

#	$\overline{T_{\text{Top}}}$ (°C)	$\overline{T_{\text{Bottom}}}$ (°C)	T_{Specific} (°C)
1	65.32 ± 0.04	39.39 ± 0.03	52.38 ± 0.23
2	65.52 ± 0.04	48.87 ± 0.04	55.91 ± 0.16
3	62.93 ± 0.05	53.68 ± 0.05	60.99 ± 0.08
Kühnel (2011)	75	30	55.36
Hallcrest	–	–	54.3 ± 1

Table 2.10.: The temperature at which the TLC R54 is visible for the green laser for different temperature ranges. The values should only deviate from each other within the error margins. The value "Hallcrest" was supplied by LCR Hallcrest, and is included here for comparison. It corresponds to the "Start of Green" value, which is nearest to (but lower than) the measurement. Measurement Kühnel (2011) is included for comparison. Other measurements were taken earlier but with limited accuracy. They are omitted here for brevity.

2.6. Laser

A light source is needed to illuminate the particles, in order to be picked up by the camera and thus by the particle tracing program. I am only interested in a 2D profile of the experimental tank, perpendicular to the camera and centred within the tank, so a narrow vertical light plane is needed. Lasers are used as the light source, because they are very bright and monochromatic,

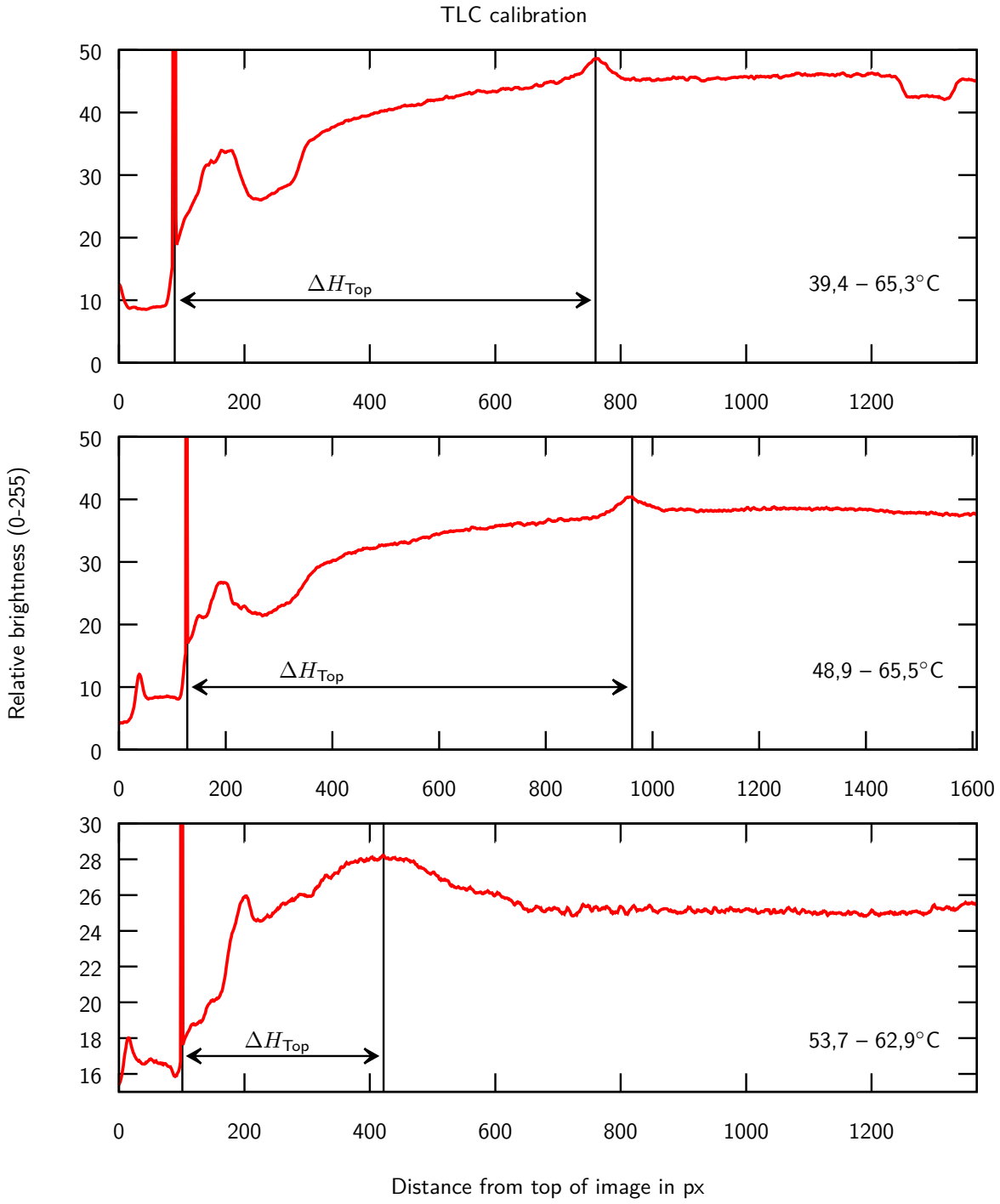

Figure 2.26.: Brightness plotted with respect to vertical position. Each graph represents a different temperature range (noted in the plots). Peaks are highlighted. The first, higher, peak is artificially created by drawing a white line onto the images, the second peak is produced by TLCs (see also Figure 2.24 on page 41). The distance between the peaks corresponds to the temperature difference and is used to calculate the temperature at the second peak.

which will be very useful during the pre-processing step. Also, it is easy to broaden a laser beam into a thin light sheet, which is necessary for PIV to work. To widen the laser beam, a diverging lens, a so called "Light Sheet Optics", is used.

Two lasers are available for the experiments presented in this work:

- A **green DPSS-MGL-III laser** by HB-Laserkomponenten with 500mW at 532nm wavelength.
- A **red shuttered CW Laser** with 1220mW at 671nm wavelength by LaVision.

The red laser is a lot more powerful than the green one, but the TLCs poorly reflect red light. That is why the red laser is not suited for remote temperature sensing. The increased brightness compared to the green one, however, helps particle tracking and therefore PIV.

Typically both lasers are used in a parallel configuration. The red laser illuminates a plane in the centre of the tank and the green one a plane several centimetres behind. Because both use different colours, these planes then can be differentiated in the pre-processing step.

2.7. Camera

Two different cameras are used for the experiments presented in this work

- A monochromatic **LaVision Imager intense** with up to 1376x1040 Pixels (1.4MP). This camera's CCD chip is cooled down to $-12°C$ and thus features a very low noise-to-signal ratio which can be further enhanced by binning. The camera takes up to 10 images/second (10Hz) and thus is especially useful for detailed studies of fast moving structures in small areas, e.g. the area just above the heating element (see 2.1 Experimental tank).
- A **Canon EOS 350D** remote controlled digital single-lens reflex camera with up to 3456x2304 Pixels (8MP), and up to 1 image every 5 seconds (.2 Hz). The high spacial and low temporal resolution makes this camera especially useful for long term evolution studies of the whole tank.

Both cameras use a 55mm lens, and are placed approximately 1m from the tank.

2.8. Scaling

It is important for the flow field in the experiments to be similar to mantle plumes, because I intend to verify a numerical model in this regime. A scaling analysis can help to estimate the laboratory flow behaviour, and thus applicability to geophysical phenomena. Important scaling factors include the Reynolds, Prandtl and Rayleigh number.

The **Reynolds Number** describes the flow regime of a fluid dynamical system. For jet flows, a critical Reynolds Number in the order of 10 is an indicator of turbulant flow, whereas a value lower than 10 is associated with laminar flow (Tritton, 1999). It is defined as

$$\mathrm{Re} = \frac{\rho \cdot v \cdot d}{\eta} \tag{2.29}$$

where ρ is the density, v the fluid's velocity, d the conduit's width and η the dynamic viscosity. To get a rough idea of the flow regime in the experiment the Reynolds Number can be estimated for the flow by approximating the parameters with

$$\rho \approx 1400\,\mathrm{kg/m^3} \qquad \text{(see 2.3.1 Density)} \tag{2.30}$$

$$v \approx 0.1 \ldots 0\,\mathrm{m\,s^{-1}} \qquad \text{for typical velocities within the plumes tail} \tag{2.31}$$

$$d \approx 0.1 \ldots 0.01\,\mathrm{m} \qquad \text{for the diameter of the plume} \tag{2.32}$$

$$\eta \approx 20 \ldots 3\,\mathrm{Pa\,s} \qquad \text{(see 2.3.4 Viscosity)} \tag{2.33}$$

and thus derive a Reynolds Number of

$$\mathrm{Re} \approx 0.7 \ldots 5 \tag{2.34}$$

suggesting laminar flow.

The **Prandtl number** is a measure for the ratio of momentum diffusivity to thermal diffusivity in a substance. The thermal diffusivity is a measure to thermal conduction while the momentum diffusion is a measure for the diffusion or spreading of momentum. In a fluid, the momentum diffusion is equal to kinematic viscosity (see 2.3.4 Viscosity). Heat transport in a system with a Prandtl number $\ll 1$ is dominated by thermal diffusivity and dominated by momentum diffusivity for $\mathrm{Pr} \gg 1$. A system in which momentum diffusion dominates is prone to vigorous thermal convection and the formation of temperature-driven plumes. Water has a Prandtl number of around 6 (Tritton, 1999) and Earth's mantle has a number of around 10^{23} (Schubert et al., 2001).

The Prandtl number is defined as

$$\mathrm{Pr} = \frac{\eta}{\rho\kappa} \tag{2.35}$$

and can be calculated for this application using

$$\kappa \approx 1.15 \cdot 10^{-7}\,\mathrm{m^2\,s^{-1}} \qquad \text{(see 2.3.3 Thermal diffusivity)} \tag{2.36}$$

$$\rho \approx 1400\,\mathrm{kg/m^3} \qquad \text{(see 2.3.1 Density)} \tag{2.37}$$

$$\eta \approx 100 \ldots 0.2\,\mathrm{Pa\,s} \qquad \text{(see 2.3.4 Falling Sphere Viscometer)} \tag{2.38}$$

and arrive at

$$\mathrm{Pr} \approx 1242 \ldots 621118 \approx 10^{3 \ldots 5} \tag{2.39}$$

The Prandtl number is obviously dependent on the temperature (mainly through the viscosity), but in any case is rather large. This suggests that thermal diffusion does not play a significant role in the main experiments, just as in Earth's mantle.

The **Rayleigh Number** is a measure for the ratio of convective heat transport to heat diffusion and can be expressed as the product of the Grasshof and the Prandtl numbers. Unstable thermal systems exhibit a high Rayleigh number and develop thermal convection. (Rayleigh–Bénard-)Instability sets in for Rayleigh numbers exceeding 1700 (Tritton, 1999). The Rayleigh number is defined as

$$\mathrm{Ra} = \frac{g\alpha\rho}{\eta\kappa}(T_{\mathrm{heating}} - T_{\mathrm{bg}})L^3 \tag{2.40}$$

With

$$g \approx 9.81\mathrm{m\,s^{-2}} \quad \text{the gravitational acceleration} \tag{2.41}$$

$$\alpha \approx 402 \cdot 10^{-6}\mathrm{K^{-1}} \quad \text{2.3.2 Thermal expansion} \tag{2.42}$$

$$T_{bg} \approx 35 \ldots 55°\mathrm{C} \quad \text{the background temperature} \tag{2.43}$$

$$T_{\text{heating}} \approx 100°\mathrm{C} \quad \text{at the heating element} \tag{2.44}$$

$$L \approx 0.4\,\mathrm{m} \quad \text{the height of the tank} \tag{2.45}$$

and ρ, η and κ from above, this computes to

$$\mathrm{Ra} \approx 10^{5\ldots8} \tag{2.46}$$

This equation only applies to infinite expanding planes, which is certainly not the case here (especially so since only the heating element is heated, not the entire bottom). Nevertheless, this yields a rough estimate and is in any case large enough to expect a vigorous thermal convection. The Rayleigh number of Earth's mantle is estimated to be in the same order of magnitude.

These calculations confirm that Earth's mantle can be expected to exhibit a similar flow regime as the plumes in the main experiments and that conclusions derived from these experiments can be applied to the mantle.

3. Experiments

3.1. Measuring methodology

To improve reproducibility and comparability, all measurements are taken using the same methodology:

Preheating

The experimental tank was heated to the desired background temperature, covered to reduce heat loss and temperature gradients, and left alone for at least 24h. During that time, the sirup's temperature comes close to isotropy.

Figure 3.1.: The empty experimental tank with its isolation removed.

Background flowfield

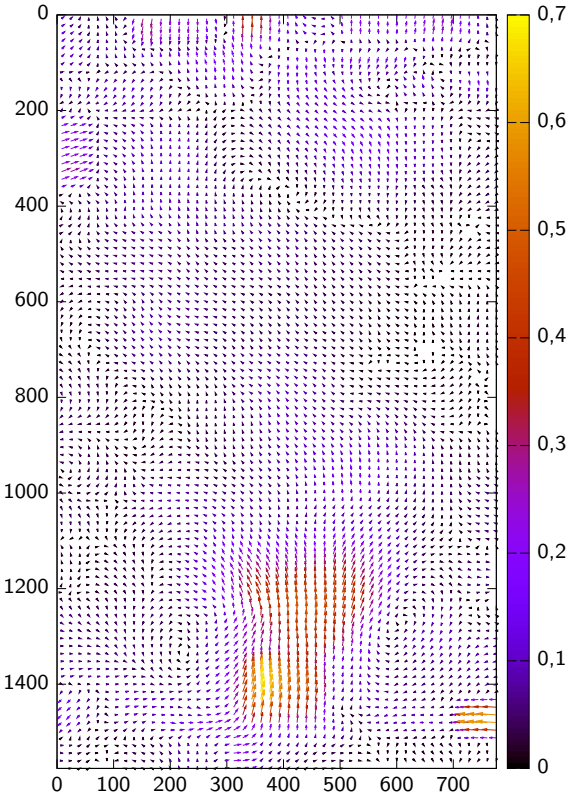

Figure 3.2.: The background flow field prior to the start of the experiment is unsteady, but lower than .7 px/frame (> 0.04 mm/s). The background flow field is strongest near the (unheated) heating element, because that is the least isolated part of the tank. Colour code in px/frame, axis in px.

Prior to the main experiment and for quality assurance, the background flow field (Figure 3.2) is measured. To this end, the cameras are set to take a reading every five seconds for ten minutes without the heating element being heated. The background flow field measurements are processed separately from the measurement.

Due to the good isolation and the constant heating by the water jacket, the background flow field is very low in all measurements. Even though the background flow field is a phenomenon not modelled by the numerical codes, its effects are negligible and thus it was not necessary to be considered in processing.

Pre-measurement preparations

The heating bath feeding the heating element is disconnected from the element and heated to the desired temperature. This avoids long internal heating times.

Measurement initialisation

Once the heating bath has reached the desired temperature the tap to the heating element is opened, the temperature measurement and the camera recording started. These events are not

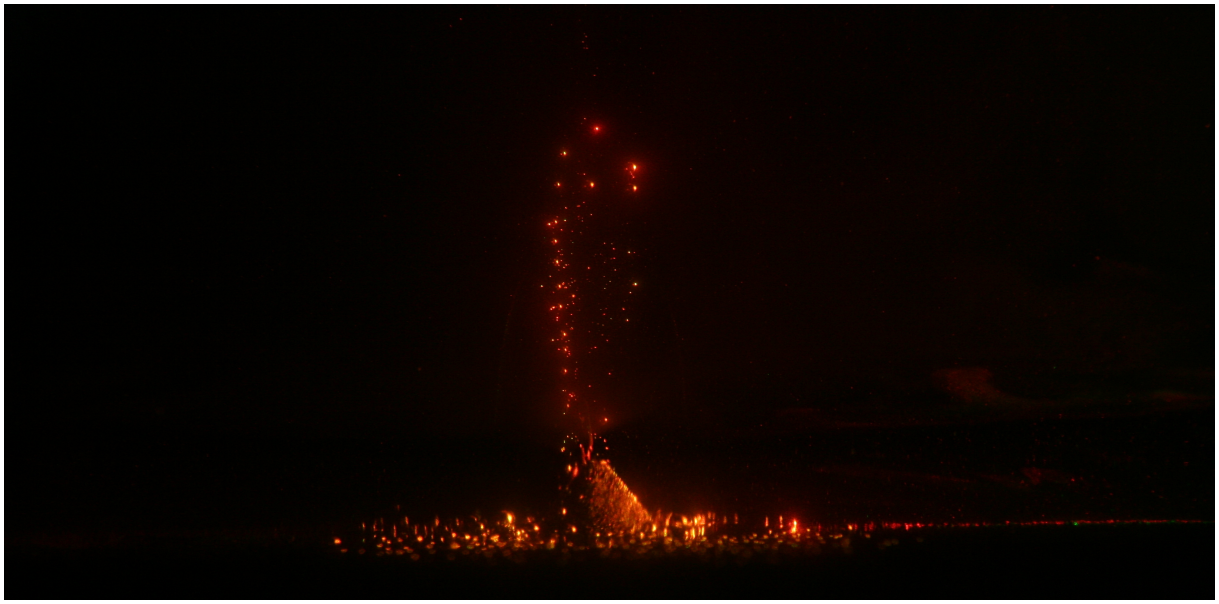

Figure 3.3.: Detail photograph of the heating element (shown for illustration only).

simultaneous, but within a timeframe of less than 20s. The cameras are automated and set to a fixed interval (.2Hz).

Within seconds of opening the tap the heating element reaches its final temperature, and a plume begins to form (Figure 3.3). It is automatically tracked by the camera system for 60–90 minutes and no manual interference is undertaken after the initialisation of the experiment. A test measurement is shown Figure 3.4 for illustration.

3.2. Summary

Thirty-six experiments were conducted of which eight were pure tests or temperature studies with no images, four suffered from instrument failure, and thirteen where foiled by air bubbles or strong background convection. Five had no temperature measurement due to technical problems. Thus five experiments remain for further processing and study. These are summarised in Table 3.1. A detailed account of all measurements can be found in the appendix (see A Main experiments).

#	$\mathbf{T}_{bg}$ (°C)	$\mathbf{T}_{heating}$ (°C)
2012-12-27	35	110
2012-12-28	35	110
2012-12-30	35	110
2012-12-12	40	110
2012-12-14	40	110

Table 3.1.: The five experiments that were used for further processing. Background and heating temperature are the temperatures set at the external heating baths. Due to heat loss the actual temperature in the tank and at the heating element is slightly lower and has to be read from the temperature measurements.

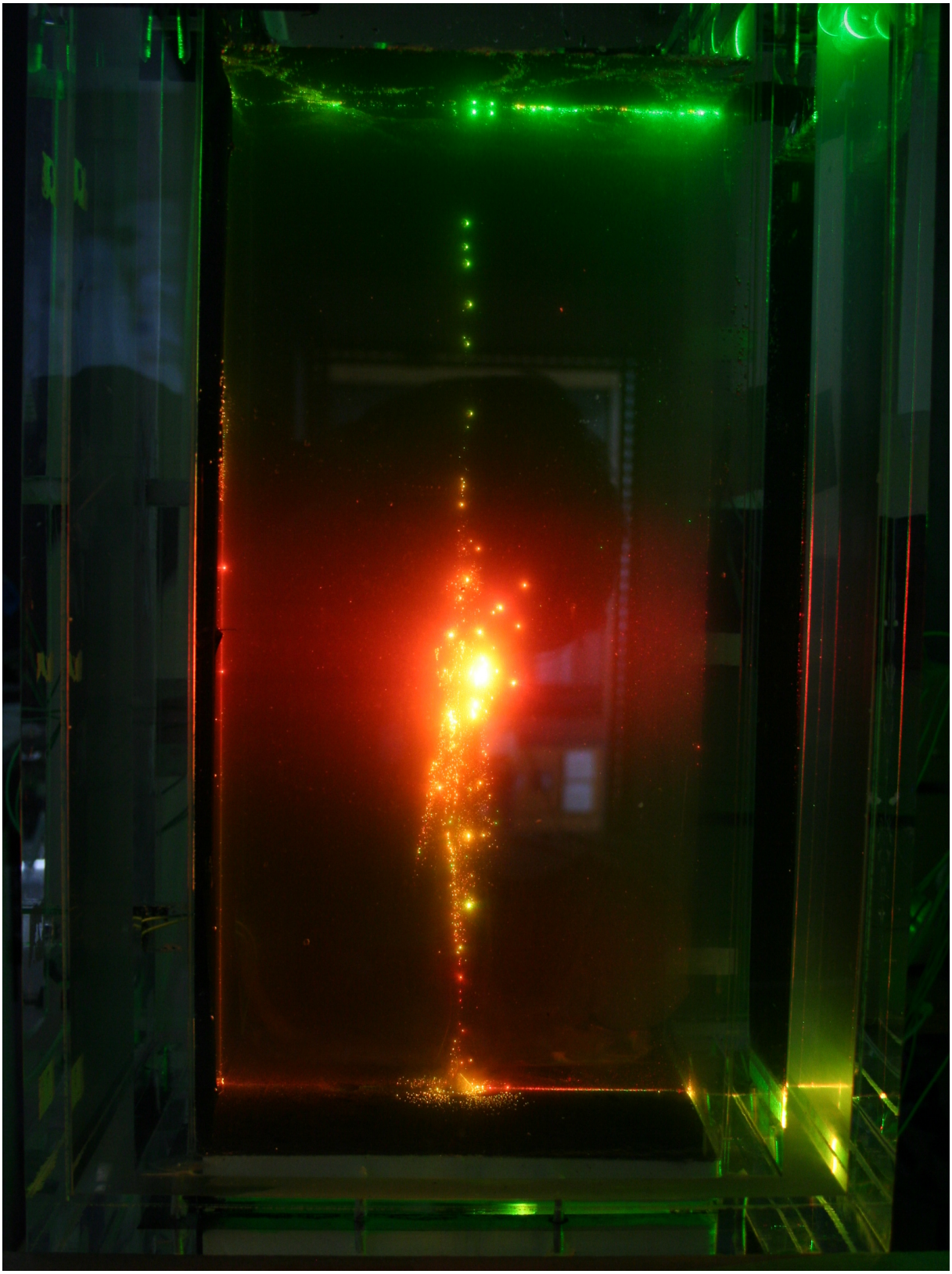

Figure 3.4.: The tank during the measurement. Not an actual measurement, but included for illustration.

4. Analysis and processing

4.1. Image preprocessing

To increase image quality the following preprocessing steps are taken (Figure 4.1 on page 52):

Step 1 To preserve the images for future studies, they are acquired in the so-called raw file format (Canon format) and converted to PNG. The raw images are archived, the PNG images are used for further processing.

Step 2 Because the camera and tank are not perfectly aligned and the camera's field of view is necessarily a bit wider than the tank, the images are rotated and cropped to show only the interior of the tank. To help with the following processing and to limit storage demands the images are scaled down to 467x819px (width times height). Tests have shown that this does not significantly affect the PIV analyses done later.

Step 3 Each image is split into its three channels (red, green, blue). Since the two lasers are red and green, I can thereby separate the two lasers and generate two different images from one.

Step 4 Because monochromatic light will still be visible on all three channels, further processing is needed. Under the assumption that red light is brightest on the red channel, green light brightest on the green channel, and blue light brightest on the blue channel, every pixel can be associated with the channel on which it is brightest. Thus, the images for the green and red channel are compared pixel-wise, and for every comparison the "weaker" pixel is blacked. In case particles coincide on the same position on both channels, this information is lost on the weaker channel. However, because the sirup is sparsely seeded and particles rarely match up perfectly, enough information is retained from the processed colour channels for PIV analysis. This processing is implemented in a very simple Matlab/octave script, which is included in the supplemental material (see 5.3 Supplemental material).

4.2. Particle Image Velocimetry (PIV)

For contactless flow field analysis, different methods are available. The most established ones are Particle Tracking Velocimetry (PTV) and Particle Image Velocimetry (PIV). As the name suggests, PTV tracks individual particles from frame to frame, while PIV tracks images (resp. parts of an image) from frame to frame. PTV requires that individual particles are well-defined and non-ambiguous, which implies a sparse, yet homogeneous seeding. PIV on the other hand

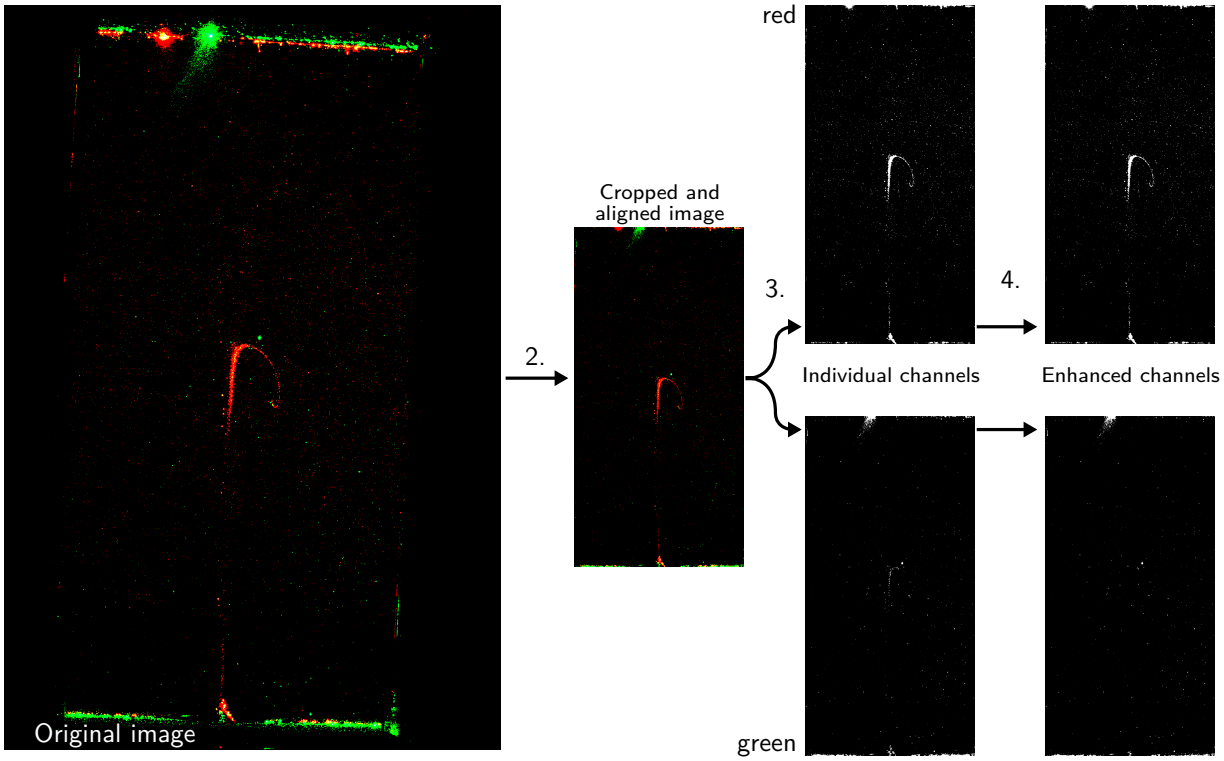

Figure 4.1.: Preprocessing steps. The images are captured as so-called raw images (Canon format) and converted to PNG (Step 1). They are aligned, cropped and reduced in size (Step 2). The channels are separated into individual images (Step 3). The channel images are enhanced (Step 4). In this figure all images are enhanced for print. Sizes are to scale.

tracks patterns, and thus requires dense seeding. PIV is more robust under less-than-ideal settings and has become the predominant method to track flow fields.

To calculate the flow field, PIV splits each frame into interrogation windows, and correlates them to windows on the next frame (known as cross-correlation). The working principle is simple (Figure 4.2 on page 53) yet the actual processing necessary is somewhat intricate.

For this work, an interrogation window size of 128x128 px (about 33x33 mm) with an overlap of 75% was used. This still produces accurate velocity readings, while being comparatively cheap in processing and disk space.

Note that PIV does not actually need discernible points, but any quasi-random pattern. In this work Silver Coated Hollow Glas Spheres are used for seeding (see 2.4 Particles).

For the flow field analysis in this work, the LaVision DaVis Software Suite is used. For an excellent description of this software and more information on PIV please review the work by Kühnel (2011). A detailed documentation of the settings used to acquire the results of this work is included in the supplemental material (see 5.3 Supplemental material).

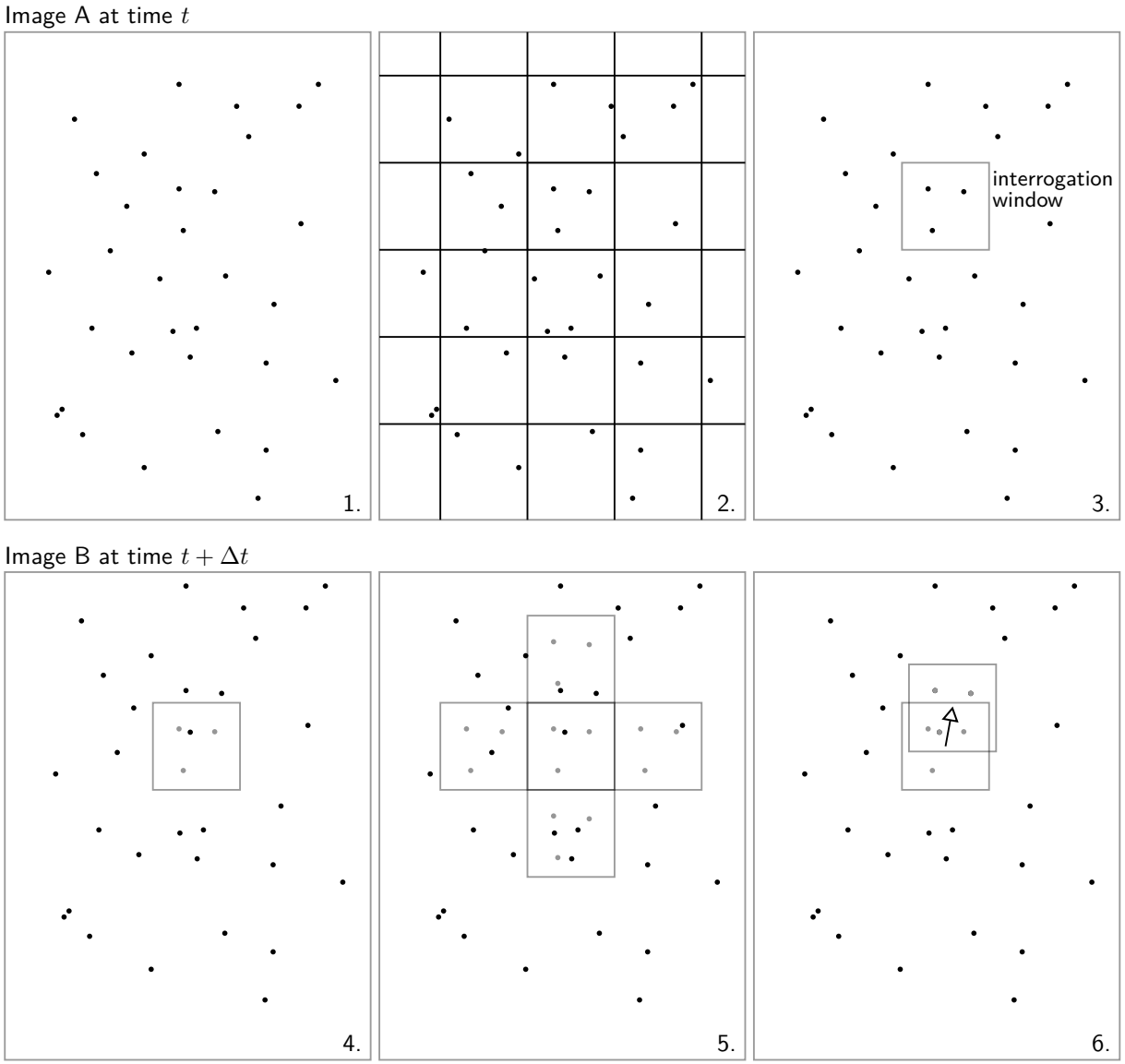

Figure 4.2.: Working principle of a PIV analysis. (1) An image of the area of interest is taken in which the flow field is to be determined. Seeding the fluid with particles is necessary to create a discernible, non-repeating pattern. (2) The image is split into windows. Each window will later be associated with a displacement vector and can be thought of as a pocket of fluid. (3) Each window is processed individually and called interrogation window. (4) On a later image, the fluid has moved, and so did the particles. The interrogation window is superimposed, but obviously, it does not "fit" well, its correlation is weak. (5) The interrogation window is superimposed on the neighbouring windows, for each superimposition, the correlation is computed resulting in a correlation function. (6) The peak of the correlation function is the place where the interrogation window fits best, and is thus the new position of the pocket of fluid. A displacement vector represents the movement. This is repeated for all windows, resulting in a field of displacement vectors which represents the flow field for the time interval between the two images.

5. Results

To objectively compare the plumes generated in the experiments with the plumes modelled in the numerical experiments, two proxy values are used: velocity profile and rate of plume ascent.

5.1. Velocity Profile

A velocity profile is a plot of absolute velocity to position. It is a useful tool to analyse one-dimensional flow fields (e.g. vertical ascent). Figure 5.1 explains the main features of a velocity profile of a plume. Measurements and numerical results are aligned at the jet region. The actual measurements are converted from px to mm and from px/frame to mm/s. For clarity, they are also rotated, so that the velocity is on the ordinate and the vertical position on the abscissa.

Figures 5.2–5.6 show the velocity profiles for the experiments in these studies, compared to the corresponding velocity profiles of modelling runs using the same temperature data.

Measurement 2012-12-12 (Figure 5.2 on page 57) clearly has an overall too high velocity field, meaning that the highest velocities within the vertical profile of the plume are higher than the highest velocities in the numerical model of the same plume. In this and the preceding experiments, air bubbles have been a major issue. Apart from interfering with PIV and resulting in very high, localised velocities (clearly visible as very high velocity peaks, e.g. measurement 2012-12-14 at 10 minutes and 150mm) they also potentially reduce the overall density of the plume and raise its buoyancy, thus increasing its driving force and speed. Because there is no equivalent mechanism in the model, it is not able to accurately predict the experimental plume.

That same effect is observable in measurement 2012-12-14 (Figure 5.3 on page 57) and 2012-12-27 (Figure 5.4 on page 58), but with continuously decreasing intensity. With every measurement, significant volumes of gas are removed from the tank (because of the high viscosity of the sirup at low temperatures, air bubbles can only escape when an experiment starts and the tank is heated from below, resulting in air bubbles being released only when measurements are taken).

In measurements 2012-12-28 (Figure 5.5 on page 58) and 2012-12-30 (Figure 5.6 on page 59) the influx of air bubbles has subsided enough to not be a significant factor in plume evolution (though single bubbles are still present).

Measurement 2012-12-30 also had an improved tank isolation, which further suppressed unwanted heat loss and decreased the deviation between the model and the measurement even further. Judging from the velocity profiles, the 2D model is capable of accurately predict the sirup plume.

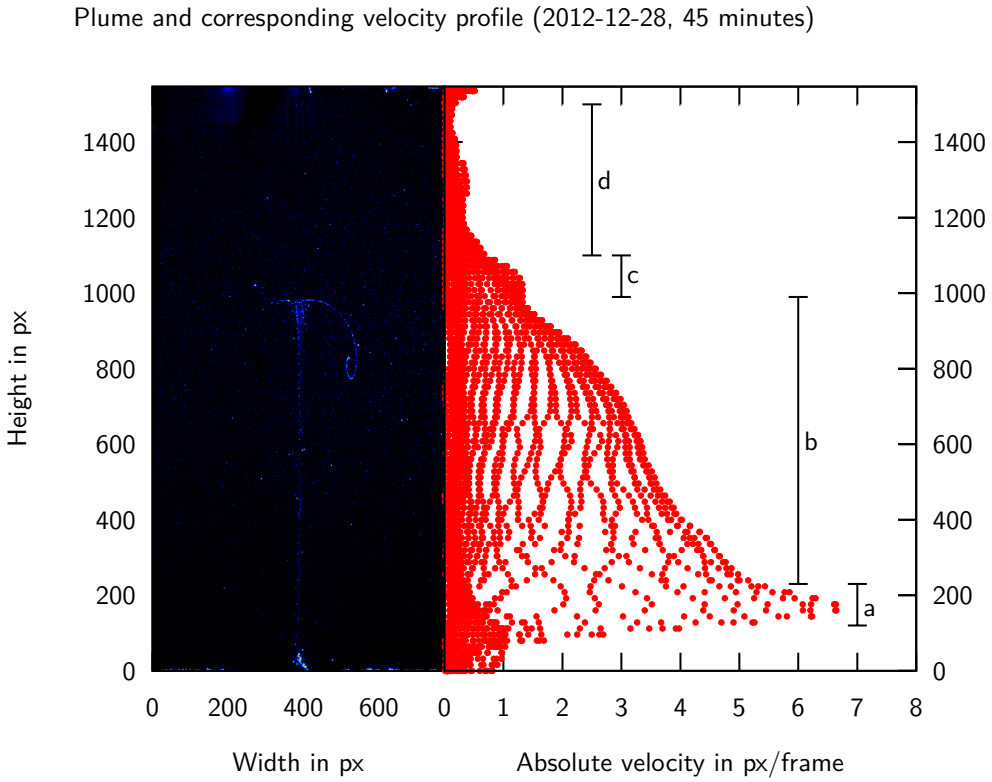

Figure 5.1.: A velocity profile plotting absolute velocity to vertical position allows to gain insight in the overall flow field. As an example, a velocity profile (on the right) for an image of a plume (on the left). Four distinct features are visible:
(a) When new (cold) material gets in contact with the heating elements, it is rapidly heated and becomes strongly buoyant. This results in a small plume jet region.
(b) The plume's tail is the main conduit through which all material goes.
(c) Plume head: The transition zone where material is slowed down and broadened into a horizontal structure.
(d) A plume-free zone where the plume has not (yet) pierced the material and velocities are near zero.

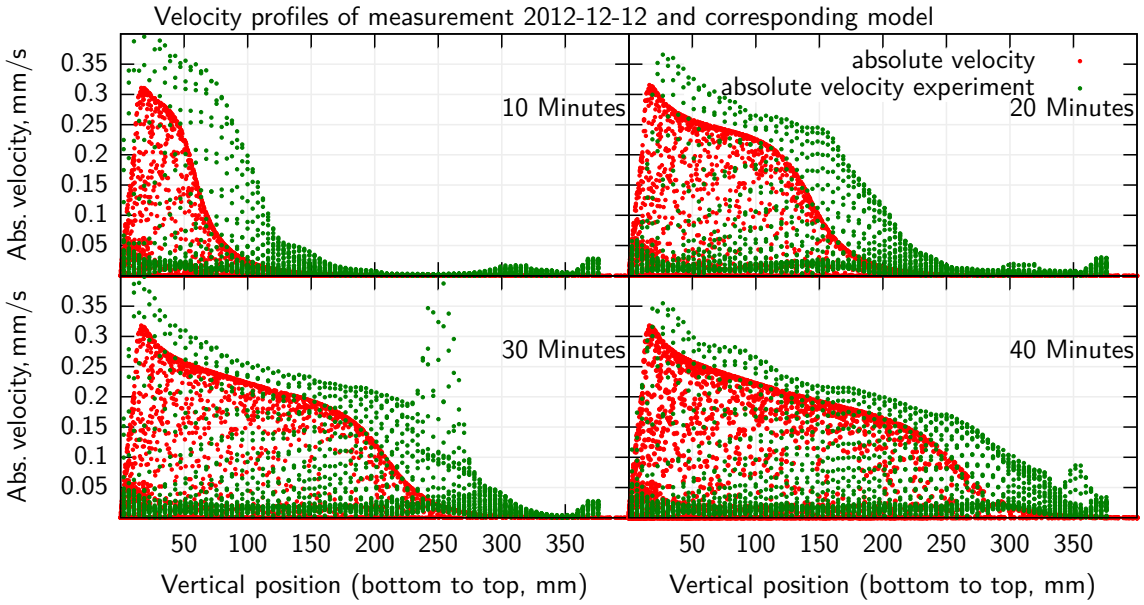

Figure 5.2.: Velocity profile of measurement 2012-12-12. Experiments in green, numerical results in red. The high velocity zone at 30 minutes and 250 mm is an ascending air bubble.

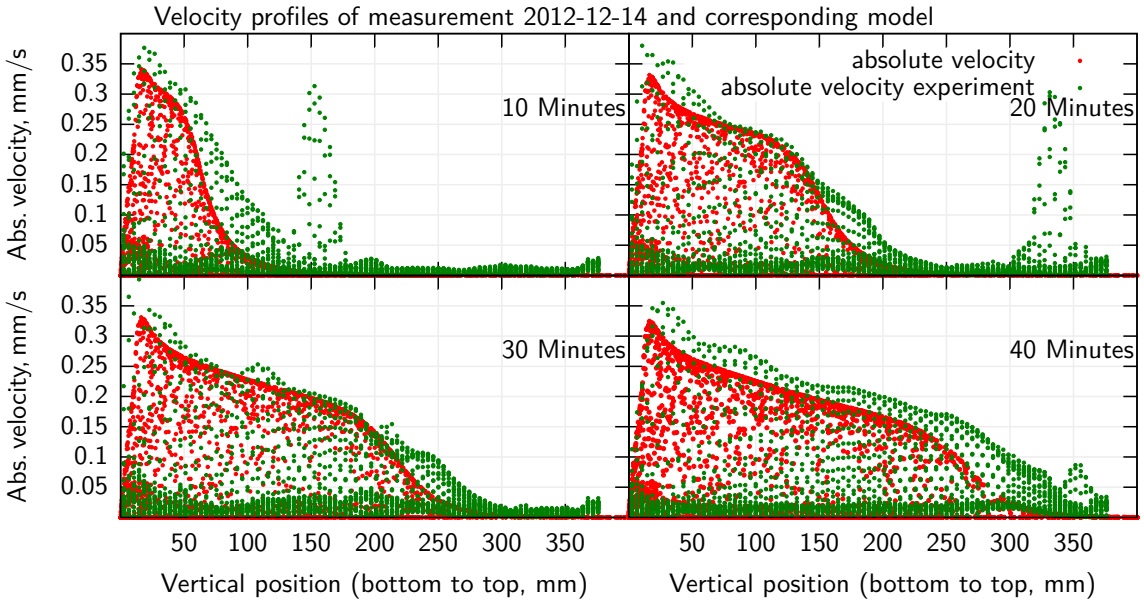

Figure 5.3.: Velocity profile of measurement 2012-12-14

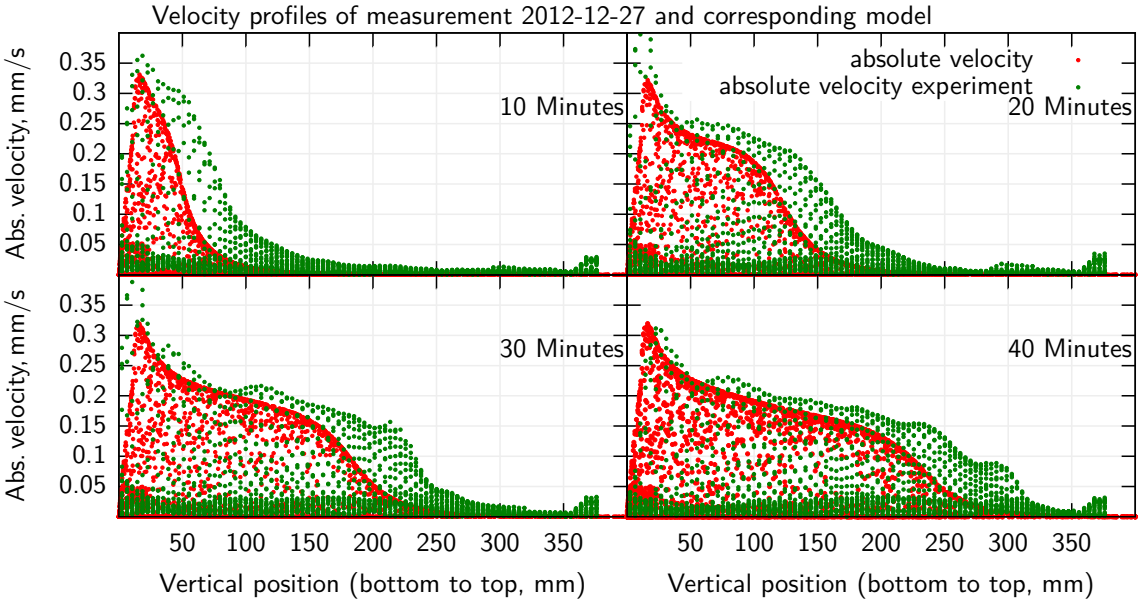

Figure 5.4.: Velocity profile of measurement 2012-12-27

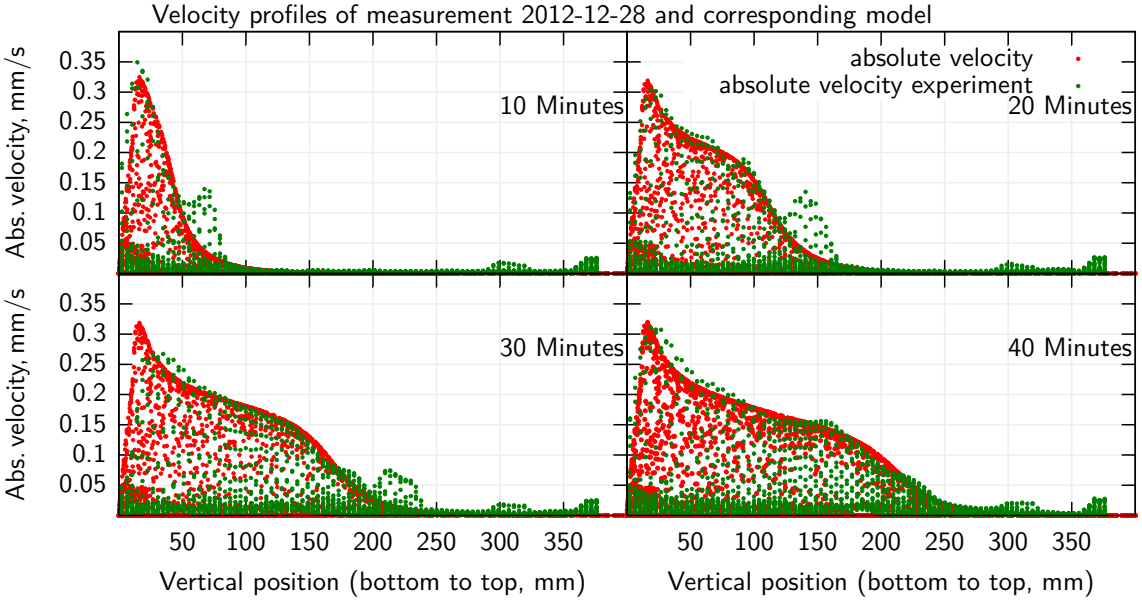

Figure 5.5.: Velocity profile of measurement 2012-12-28

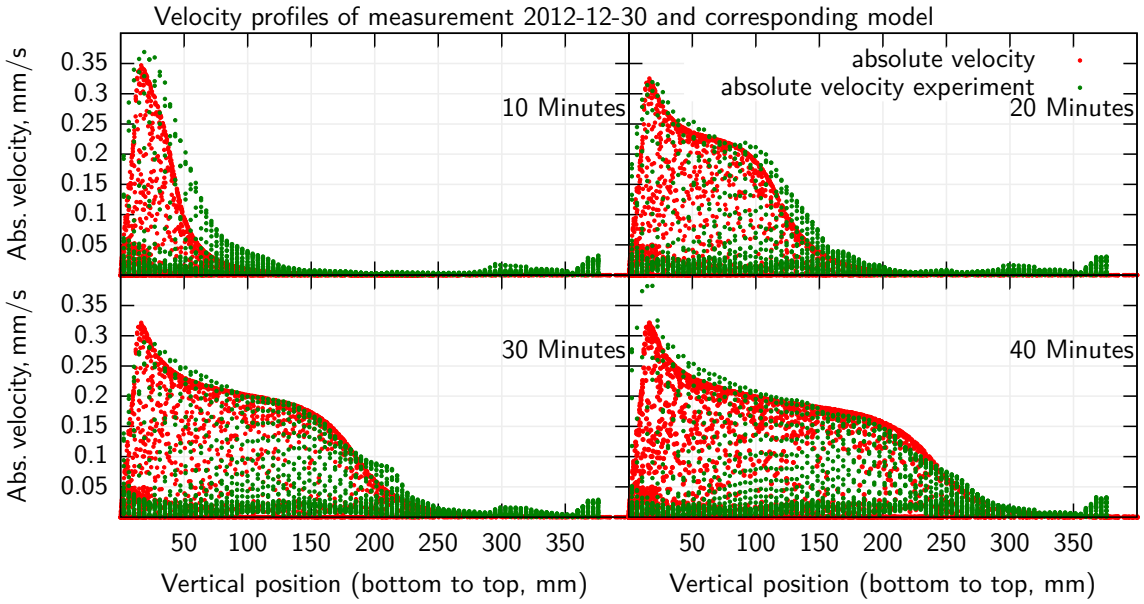

Figure 5.6.: Velocity profile of measurement 2012-12-30

5.2. Plume ascent

From the velocity distribution within the tank the plume height can be derived. Measuring the plume's height at different times yields the plume's ascent rate, which can be used as an additional proxy value for plume similarities between laboratory experiment and numerical model.

Since the plume should generate the entire flow field in the tank, the height of the plume can be found by defining a threshold velocity. Where this threshold is met or exceeded, the plume exits. An arbitrary minimum velocity of 0.05 mm/s[1] has been set, which is above the noise in the measurements but small enough to detect plume edges. Figure 5.7 illustrates the height measurement.

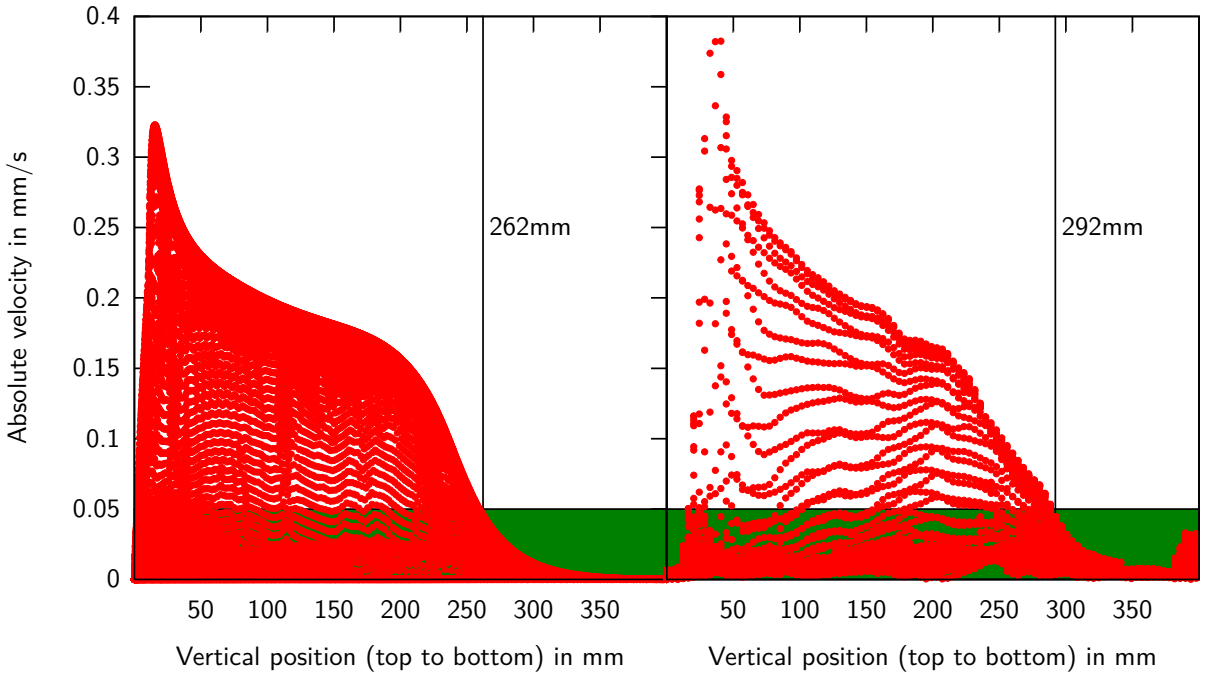

Figure 5.7.: How the plume height is determined. A threshold value (green) is set to cut off background noise. The height is then the intersection of the envelope of the velocity field and the threshold value.

Figure 5.8 shows the ascent rates for all measurements. As with the flow field, the measurements show a clear deviation for 2012-12-12, 2012-12-14 and 2012-12-27, but the rate of ascent (=velocity) is very similar. Both 2012-12-28 and 2012-12-30 show a very good fit between the modelled and the measured plume.

[1] Or $\frac{1}{220000}$ of the airspeed velocity of an unladen swallow.

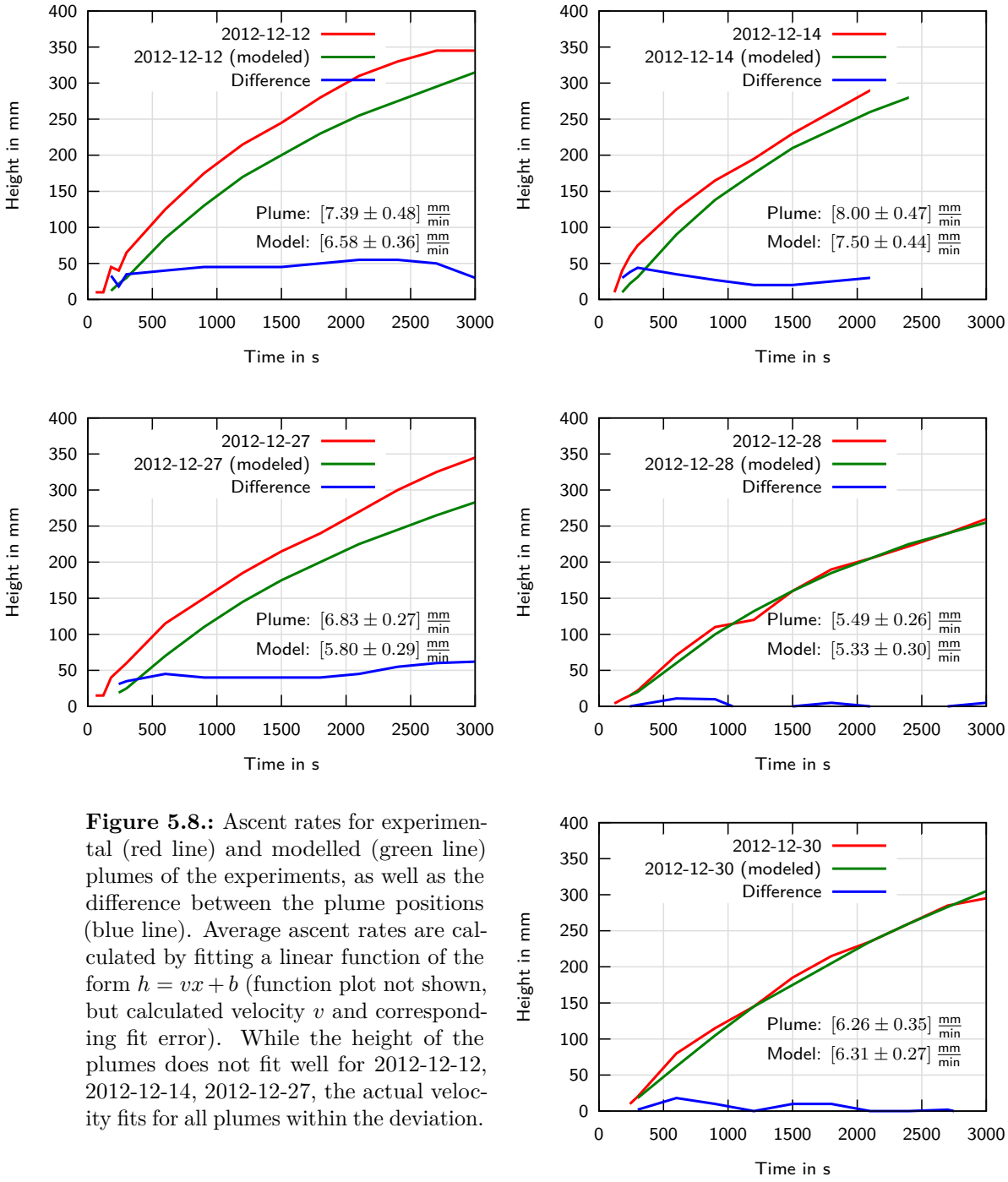

Figure 5.8.: Ascent rates for experimental (red line) and modelled (green line) plumes of the experiments, as well as the difference between the plume positions (blue line). Average ascent rates are calculated by fitting a linear function of the form $h = vx + b$ (function plot not shown, but calculated velocity v and corresponding fit error). While the height of the plumes does not fit well for 2012-12-12, 2012-12-14, 2012-12-27, the actual velocity fits for all plumes within the deviation.

5.3. Supplemental material

The data (see 3 Experiments) generated in this work is available as a processed data set. This supplementary material includes the original raw data, the calculated flow field data from PIV, the temperature data as well as a corresponding 2d model run. All codes used to process and generate the data set is included and additional documentation is provided.

The supplementary material can be obtained from the Institute of Geophysics, University of Hamburg.

6. Discussion & Outlook

As discussed in the previous chapter, the measurements were faithfully reproduced by the M2TRI model. This serves as good evidence that the M2TRI model is correct in this regime, and that this is a viable approach. It will be interesting to compare the measurements to the M3TET model as well, which will be done in the near future. For this, the second plane that was measured, but not further explored, will be useful.

Interestingly, non of the measurements at or above 50°C background temperature did produce the expected plumes. These experiments resulted in complex flow behaviours: initially well-formed plumes got stuck, disintegrated, pulsed, and even separated into quasi-independent fragments. This could be an interesting starting point for studies of complex plume formations at low temperature gradients.

Air bubbles were one of the major problems in these (and prior) studies and are the main reason for inaccurate experiments. It is obvious that these bubbles contribute significantly to plume formation and evolution. Since they are not included in the numerical codes, any measurement burdened with bubbles cannot be faithfully reproduced. If this problem is addressed, more accurate and reliable measurements can be taken which will allow a more in-depth and precise analysis of the numerical plumes.

When comparing the numerical results to the experiments, it becomes obvious that the deciding parameters for the numerical modelling are viscosity and the boundary conditions at the heating element. Future studies should concentrate on these parameters. The sirup's viscosity changes from sample to sample and over time, and should therefore be measured for every tank-filling independently. The venerable falling ball viscometer has proven to be a very reliable, simple and comparatively cheap instrument to work with, and is ideally suited for these kind of studies.

Unfortunately, the temperature measurement through TLCs did not succeed, which would have yielded an additional and independent proxy for plume comparison, and would be an important constraint for modelling. Why the TLCs never fully worked is unclear, but might be a combination of not-ideal concentration, an unsuitable type of TLCs, ageing effects and a not powerful enough laser.

Mixing the TLCs into the sirup has been one of the major hurdles. Mixing laminar fluids like sirup is extraordinary difficult to do by hand, and machinery tends to entrain large amount of air that, due to the viscous nature of sirup, does not escape at a reasonable rate. Heating the sirup helps alleviate these problems to a degree, but brings about the hazard of burning, and makes handling difficult.

It is regrettable that the TLCs in use are not visible with the second (red) laser. A different type of TLCs might potentially be usable with the red laser, opening new applications. For example, two lasers could be used in tandem configuration, illuminating the same plane in the tank. That would yield twice the number of isoterms to be detected.

Apart from the obvious problem of TLC concentration, the calibration of TLCs can be improved by using a better experimental setup. Precise measurements of TLC lines could also provide a temperature range of TLC visibility, which could be used to assess the local thermal gradient.

The thermocouple data is not further explored in this work because it does not yield much additional information. It is however used directly in the numerical codes to create the numerical plumes. The data is included in the supplemental material.

Finding a good concentration for particles is not straight-forward either. PIV needs patterns of particles to find correlation between frames, but too many particles dim and diffuse light. I suspect that the pattern generated through TLCs might suffice for PIV analysis which would remove the need for additional seeding and improve overall brightness.

Apart from "just" improving these kinds of experiments, there are many conceivable variations: mantle wind (a constant drift in the whole body of the fluid) and overriding plates are obvious, but it would be even more insightful to model compositional effects which generate the 410 and 660 km discontinuities in Earth's mantle. These play a pivotal role in mantle plume evolution. It is conceivable—while demanding for the experimentator—that a layered sirup approach, where different types of sirup are layered above each other, could be employed to study the effects of viscosity changes and intermittent interfaces. Insights into plume behaviour at intermittent interfaces would yield information that is not currently available and would be a promising the next steps for these experiments.

Acknowledgement

First and foremost, my sincere gratitude goes to my advisers Matthias Hort and Jörg Hasenclever, who had the patients I needed and whom I would be glad to work with in the future. I would like to extend my thanks my friends Jonathan, Julia, Katja, Lucia and Sahar for their meticulous inspection, scrutiny and everything they deemed to be "unscientific".

I would also like to thank Donald Knuth for TEX and all the people designing and writing LATEX — I had all the fun I never wanted to have.

List of Figures

List of Tables

Bibliography

Allen, R. M. (2002). Imaging the mantle beneath Iceland using integrated seismological techniques. *Journal of Geophysical Research*, 107(B12):2325.

Dantec Dynamics (2013). Seeding Materials. `http://www.dantecdynamics.com/seeding-materials`.

Davaille, A., Limare, A., Touitou, F., Kumagai, I., and Vatteville, J. (2011). Anatomy of a laminar starting thermal plume at high Prandtl number. *Experiments in Fluids*, 50(2):285–300.

Davaille, A. and Vatteville, J. (2005). On the transient nature of mantle plumes. *Geophysical Research Letters*, 32(14).

Elert, G. (2013). The Physics Hypertextbook - Thermal Expansion. `http://physics.info/expansion/`.

Evans, D. and Morriss, G. (1988). Transient-time-correlation functions and the rheology of fluids. *Physical Review A*, 38(8):4142–4148.

Evonik Industries (2013). VESTOSINT® 1111 naturfarbe. `http://www.vestosint.de/sites/dc/Downloadcenter/Evonik/Product/VESTOSINT/de/produktinformationen/Produktinformation_VESTOSINT_1111naturfarben.pdf`.

Hasenclever, J. (2010). *Modeling Mantle Flow and Melting Processes at Mid-Ocean Ridges and Subduction Zomes – Development and Application of Numerical Models*. PhD thesis, Universität Hamburg.

Hasenclever, J., Morgan, J. P., Hort, M., and Rüpke, L. H. (2011). 2D and 3D numerical models on compositionally buoyant diapirs in the mantle wedge. *Earth and Planetary Science Letters*, 311(1-2):53–68.

Kühnel, M. (2011). Analog Laboratory Experiments on thermal Anomalies. Master's thesis, Universität Hamburg.

Limare, A., Kumagai, I., Vatteville, J., and Davaille, A. (2008). Thermal plumes visualisation: differential interferometry versus thermochromic liquid crystals. In *13th International Symposium on Flow Visualization*.

Lohmann, F. C. (2005). *Entrainment Processes during Plume Ascent*. PhD thesis, Christian-Albrechts-Universität zu Kiel.

Machetel, P. and Weber, P. (1991). Intermittent layered convection in a model mantle with an endothermic phase change at 670 km. *Nature*, 350(6313):55–57.

Mende, D. and Simon, G. (1975). *Physik: Gleichungen und Tabellen*. VEB Fachbuchverlag Leibzig, 5 edition.

Morgan, W. J. (1971). Convection Plumes in the Lower Mantle. *Nature*, 230(5288):42–43.

Nataf, H. (2000). Seismic imaging of mantle plumes. *Annual Review of Earth and Planetary Sciences*, (1971):391–417.

Ricard, Y. (2007). Physics of mantle convection. *Treatise on Geophysics*.

Schott AG (2013). Glass Powder Technology. `http://www.schott.com/epackaging/english/overview/technologies/powder.html`.

Schubert, G., Turcotte, D. L., and Olson, P. (2001). *Mantle Convection in the Earth and Planets*. Cambridge University Press.

Smith, R. B., Jordan, M., Steinberger, B., Puskas, C. M., Farrell, J., Waite, G. P., Husen, S., Chang, W.-L., and O'Connell, R. (2009). Geodynamics of the Yellowstone hotspot and mantle plume: Seismic and GPS imaging, kinematics, and mantle flow. *Journal of Volcanology and Geothermal Research*, 188(1-3):26–56.

Tritton, D. J. (1999). *Physical fluid dynamics*, volume 50.

Vatteville, J., van Keken, P. E., Limare, A., and Davaille, A. (2009). Starting laminar plumes: Comparison of laboratory and numerical modeling. *Geochemistry, Geophysics, Geosystems*, 10(12).

Wolfe, C., Bjarnason, I., VanDecar, J., and Solomon, S. (1997). Seismic structure of the Iceland mantle plume. *Nature*.

Appendices

A. Main experiments

Table A.1.: All main experiments. Not all measurement were used to further processing, those who were are printed in bold font and listed in chapter 3 Experiments. Note that $T_{heating}$ corresponds to the temperature as set in the heating bath connected to the heating element. The actual temperature of the element is lower due to head loss in the tubing and elsewhere. It is measured as part of the temperature logging. The same applies for the background temperature.

Date	T_{bg} in °C	T_{heat} in °C	Frequency	Comment
2012-10-05			.2Hz	Test run
2012-10-08	45	65	1/60 Hz	Plume fails to form
2012-10-10	35	70	1/120 Hz	
2012-10-12	35	90	.1Hz	Strong background flow
2012-10-24	35	110	.1Hz	Strong background flow
2012-11-08	35	110	.2Hz	Air bubbles
2012-11-14	35	110	.2Hz	Air bubbles
2012-11-15	40	110	.2Hz	Air bubbles
2012-11-16	45	110	.2Hz	Air bubbles
2012-12-01	45	110	.2Hz	Air bubbles; no temperature measurement (Instrument failure); RAW data missing
2012-12-03	45	110	.2Hz	Air bubbles
2012-12-04	45	110	.2Hz	Air bubbles; No temperature measurement (Instrument failure)
2012-12-05	45	110	.2Hz	Air bubbles; First measurement with preheated heating element
2012-12-06	45	110	.2Hz	Air bubbles
2012-12-10	40	110	.2Hz	long term temperature study without camera
2012-12-12	**40**	**110**	**.2Hz**	

Continued on next page

Table A.1 – *Continued from previous page*

Date	T_{bg} in °C	T_{heat} in °C	Frequency	Comment
2012-12-13	40	110	.2Hz	failed measurement, no plume head, unreasonable large initial velocity
2012-12-14	**40**	**110**	**.2Hz**	
2012-12-26	35	110	.2Hz	Detailed temperature study with probes 3, 4 and 10
2012-12-27	**35**	**110**	**.2Hz**	
2012-12-28	**35**	**110**	**.2Hz**	
2012-12-30	**35**	**110**	**.2Hz**	**New insulation**
2013-01-04	55	110	.2Hz	Camera failure after 65 minutes; plume looses boyancy and collapses
2013-01-06	55	110	.2Hz	No temperature measurement (Instrument failure); plume looses boyancy and collapses
2013-01-07	55	110	.1Hz	No temperature measurement (Instrument failure); plume looses boyancy and collapses
2013-01-09	55	110	–	No temperature measurement (Instrument failure); Experiment aborted
2013-01-10	55	110	.1Hz	No temperature measurement (Instrument failure); plume looses boyancy and collapses
2013-01-11	55	110	.1Hz	No temperature measurement (Instrument failure); plume looses boyancy and collapses
2013-01-18	55	110	.2Hz	No temperature measurement; plume looses boyancy and collapses
2013-01-30	50	110	.2Hz	Experiment aborted due to camera failure
2013-03-20	**35**	**100**	**.2Hz**	
2013-03-21	**40**	**100**	**.2Hz**	
2013-03-25	40	100	1/30Hz	Test measurement
2013-03-27	40	100	.2Hz	
2013-03-28	40	40	1/30 Hz	Experiment aborted
2013-04-03	40	100	.2Hz	Plume gets stuck

B. Sirup

B.1. Datasheet Sirup

Glukosesirup 43

Beschreibung:

Gereinigte und konzentrierte wässrige Lösung von zur Ernährung geeigneten, aus Stärke gewonnenen Sacchariden.

CAS Nr.: 8029-43-4
EINECS : 232-436-4

Spezifikation:

* Physikalisch chemische

Aussehen	sirupartige, farblose bis gelbliche Flüssigkeit	
Geschmack	süß	
Geruch	neutral	
Brix-Wert bei 20°C	MCL 001A	81,1 - 82,1
Brechungsindex	MCL 001A	1,4936 - 1,4962
Trockensubstanz	MCL 006A	78,9 - 79,8%
DE-Wert	MCL 050B	40 - 43
Sulfatasche	MCL 255A	max. 0,1%
pH in Lösung	MCL 020B	4,5 - 5,5
SO2	MCL 060P	max. 10 ppm

* Mikrobiologische

- Aerobe Keime	MMC 2002A	max. 1000/g
- Hefen	MMC 2003A	max. 50/g
- Schimmelpilze	MMC 2003A	max. 50/g
- E.Coli	MMC 2009A	abwesend in 1g
- Salmonellen	MMC 2010	abwesend in 10 g

B.2. Datasheet Sirup

Richtwerte

Kohlenhydrat-Zusammensetzung	MCL 190A	
- Glukose	ca. 18%	
- Disaccharide	ca. 14%	
- Höhere Polysaccharide	ca. 68%	
Viskositäten		
- 20° C		ca. 100 000 mPa.s
- 30° C		ca. 30 000 mPa.s
- 40° C		ca. 9 000 mPa.s
- 50° C		ca. 4 000 mPa.s
Dichte	bei 40° C	ca. 1,41
Nährwertangabe Brennwert, pro 100g Handelsware		1349 kJ (317 kcal)

Zulassung:

- Richtlinie des Rates der EG-2001/111/EG (Amtsblatt EG L- 10 vom 12/01/2002).
- CODEX STAN 212 - 1999
- US code of Federal Regulations 21 CFR § 168-120
- FOOD CHEMICALS CODEX, 4. Ausgabe

Lagerung:

Standartverpackungen:	Tankwagen, 300 kg Stahlfass.
Optimales Haltbarkeitsdatum:	Herstellungsdatum + 24 Monate

Fassung vom 31.01.2005

Wir geben diese Produktspezifikation als Großhandel in Abschrift der Herstellerangaben weiter.

Eidesstattliche Erklärung

Hiermit versichere ich, dass ich die vorliegende Diplomarbeit selbstständig und ausschließlich unter Verwendung der angegebenen Literatur und Hilfsmittel verfasst habe. Alle Stellen, die wörtlich oder sinngemäß aus Veröffentlichungen entnommen wurden, sind als solche kenntlich gemacht. Diese Versicherung bezieht sich auch auf alle in der Arbeit enthaltenen Abbildungen. Diese Arbeit wurde bisher keiner anderen Prüfungsbehörde vorgelegt.

Ich stimme einer etwaigen Veröffentlichung zu.

Johann Jacobsohn